Mindlin-Reissner plate formulation with enhanced kinematics: Theoretical framework and numerical applications

Ibrahim Bitar, Benjamin Richard

Mindlin-Reissner plate formulation with enhanced kinematics: Theoretical framework and numerical applications

Ibrahim Bitar[1 a,b], Benjamin Richard[b]

[a]*DEN - Service d'Études Mécaniques et Thermiques (SEMT), CEA, Université Paris-Saclay, Gif-sur-Yvette F-91191, France*
[b]*IRSN, SES, Laboratoire de Modélisation et d'Analyse de la Performance des Structures, Fontenay aux Roses F-92260, France*

Abstract

This paper presents a kinematic enhanced plate model formulated within the *Mindlin-Reissner* theory. The main purpose of the model is to simulate the behavior of a structure up to membrane or bending failure. The shear strain is taken into account and the numerical shear locking problem is regularized by the *Assumed Transverse Shear strain Field* method. Two kinematic enhancements are applied at the level of the displacement fields by introducing two strong discontinuity fields. The first one is associated with the membrane displacement field and allows to describe the membrane failure and the second one is introduced in the rotation field to describe the bending failure. The *Embedded Finite Element Method* is used to incorporate the two kinematic discontinuities within a plate finite element, which allows to determine these new variables at the local level by the static condensation technique and to keep the architecture of the computational software unchanged. The kinematic and equilibrium operators associated with the enhancement variables are determined by fulfilling specific conditions. Case-studies are considered to asses the relevancy of the behavior of the enhanced membrane component as well as the behavior of the enhanced bending component. A mesh sensitivity analysis is also carried out. Finally, the Willam's test is performed for both components to verify the numerical robustness of the model and to analyze the apparent anisotropy associated with the development of discontinuities within the element. The present results allow to demonstrate the robustness of the numerical framework reported in this paper.

Keywords: Plate Finite Element, shear locking, strong discontinuities, E-FEM, membrane failure, bending failure

1. Introduction

When studying a solid mechanics problem, the choice of kinematic assumptions allows to particularize it for specific applications. A plate model is a solid structure element characterized by a reference plane and by a thickness, which is small compared to other dimensions (length and width). It can be made of a homogeneous material or of different layers of different materials. In addition, this framework is derived from the plane cross-section hypothesis and introduces, besides displacements, the notion of cross-section rotations. The *Kirchhoff Plate* (KP) theory is widely used for thin structures for which shear effects are negligible. On the other hand, the *Mindlin-Reissner Plate* (MRP) theory is used for any structure and particularly thick ones, whose transverse shear strain is of great importance and needs to be taken into account [1]. Regarding finite element discretization, the MRP variational formulation is more flexible than the KP formulation since the displacement field can be approximated by C^0 interpolations. However, plate elements belonging to the MRP theory are sensitive to the so-called shear locking, when the plate tends to be very thin. This problem has been widely studied in the literature and in this paper the *Assumed Transverse Shear strain Field* method is used to overcome this drawback.

1. Corresponding author: Ibrahim Bitar (ibrahim.bitar@irsn.fr)
To cite this paper:
Bitar, Ibrahim and Benjamin Richard. 2019. Mindlin-Reissner Plate Formulation with Enhanced Kinematics: Theoretical Framework and Numerical Applications.Engineering Fracture Mechanics, Volume 225, 2020, 106839, ISSN 0013-7944, https://doi.org/10.1016/j.engfracmech.2019.106839.

Nomenclature

$\mathbf{d}_e$	Elementary displacement vector
$\mathbf{K}_e$	Elementary stiffness matrix of a plate element
$\mathcal{H}$	The Heaviside function
$\overline{\overline{\mathbf{d}}}_e$	Elementary discontinuity vector
$\overline{\overline{\mathbf{U}}}_e$	Displacement discontinuity vector
$\mathbf{B}$	Matrix of the first derivatives of the interpolation functions
$\mathbf{C}$	Local stiffness matrix
$\mathbf{D}$	Matrix of stiffness of the plate cross-section
$\mathbf{e}$	Membrane strain component field
$\mathbf{F}$	Plate generalized force field
$\mathbf{G}_r$	Compatibility operators
$\mathbf{G}_v$	Equilibruim operators
$\mathbf{N}$	Matrix of interpolation functions
E	Young's modulus
G_f	Fracture energy in bending
G_m	Fracture energy in membrane
M_u	Ultimate stress value in bending
N_u	Ultimate stress value in membrane
$\mathbf{U}$	Generalized displacement field
$\mathbf{u}$	Displacement field
$\boldsymbol{\varepsilon}$	Plate generalized strain field
$\boldsymbol{\epsilon}$	3D strain field
$\boldsymbol{\gamma}$	Shear strain component field
$\boldsymbol{\kappa}$	Bending strain component field
$\boldsymbol{\sigma}$	3D stress field
$\boldsymbol{\Theta}$	Rotation field
ν	Poisson's ratio
$\overline{\overline{\boldsymbol{\Theta}}}_e$	Rotational discontinuity vector
δ	The Dirac function

The (MRP) theory is used in the literature to model structures of different scales. For instance, [2] extended this theory to capture the microstructure and thus the size effect in the context of functional gradation microplates. However, in our work, we are more interested in large-scale structures, particularly reinforced concrete walls and slabs. This work aims to develop an MRP plate element allowing to model properly the strain-softening phenomena that accompanies cracks initiation prior to the element failure. To achieve this objective, three main strategies are proposed in the literature: (i) the *smeared crack strategy*, in which the assumption of a continuous model is made by its stress-strain relationship and thus, the representative displacement jump is replaced by an equivalent inelastic strain. The main problem with this strategy is that cracking features can not be quantified; (ii) the *discrete crack strategy*, in which the strain softening is modeled by means of kinematic enhancements. In addition, cracks are modeled by interface (zero-thickness) elements placed between two adjacent finite element. This strategy does not require a very fine mesh, but localized failure can only occur in predetermined locations. Re-meshing is often necessary to follow the propagation of the crack [3]; (iii) in this paper, the focus is on a third strategy entitled the *discontinuous crack strategy*. The principle is to incorporate the kinematics associated with the small scale at the material level with the

kinematics associated with the large scale at the structure level. The discontinuity is termed as weak when it is introduced in the strain field while it is strong when it is introduced in the displacement field. The discontinuity can be taken into account according to different finite element methods: (a) the *Extended Finite Element Method* (X-FEM), in which discontinuities are carried out by nodes and solved at the global level [4, 5]. (b) the *Embedded Finite Element Methods* (E-FEM), in which discontinuities are not restricted to the element boundaries, nor held by nodes, but embedded within the element [6]. This technique allows determining the displacement discontinuities at the local level of the element using static condensation technique without changing the number of degrees of freedom to be resolved globally at the structure level. The application of the discontinuity crack strategy on plate structures is initiated by [7] where a hinge line is embedded within the rotation field. In [8], a multiscale approach is presented to model strain localization by means of concentrated hinge lines in plates elements using E-FEM for which two displacement jumps in the rotation and deflection fields were considered in contrast to the model proposed here. Indeed, the proposed model in the present paper consists in enhancing the displacement and rotation fields of the plate element by a membrane and a rotational discontinuities respectively, within the E-FEM scope. This choice is more appropriated to deal with civil engineering application, in which bending is a common loading. On the other hand, failure under antiplane conditions was analysed by [9].

To find a numerical solution to the problem, the equilibrium equations are first linearized in order to illustrate how they can be implemented. Case-studies are presented to verify the relevancy of the model. First, the opening and closing mechanisms of each discontinuity is checked under cyclic loading. Then, we examine the case for which the two discontinuities of membrane and rotation are activated at the same pseudo-time without ensuring a specific coupling between them. Furthermore, a sensitivity analysis with respect to the mesh size is carried out to show that the model is free of mesh-dependency effects.

Finally, a particular attention is paid to the Willam's test. This test aims to check not only the robustness of the numerical integration strategy but also to study the capability of the model to describe the intrinsic anisotropy when non proportional loading is considered. The test is performed for both membrane and rotation discontinuities. The numerical implementations as well as the various cases studied were carried out in CastLab toolbox [10].

The paper is organized as follows. Section (2) recalls the main ingredients for formulating a MRP element with the appropriate kinematic assumptions. The displacement and strain fields are introduced. The variational formulation is then addressed within the framework of the principle of virtual works. Then, the generalized behavior model of the plate structure is derived from a behavior relationship of an isotropic elastic material. The *Assumed Transverse Shear Strain Field* method to prevent from shear locking problem is also briefly examined. In section (3) the kinematic enhancement of the plate is detailed. The two discontinuities of membrane and rotation are introduced. In addition, generalized cohesive models representing discontinuities behaviors are examined. The compatibility and equilibrium operators are determined in section (3.4). Section (4) is devoted to the linearization procedure of the equilibrium equations. Finally, different case studies are examined to verify the proper functioning of the enhanced model.

2. Plate finite element modeling

2.1. Kinematic assumptions

Let us consider a plate structure having a thickness of h as shown in Fig.1. We start by pointing out that the spatial coordinates (x, y) in the plane are designated by the vector $\mathbf{x}$; in addition, the out-of-plane coordinate, z, remains scalar [2]. The displacements u_x and v_y of any point P of coordinates $(\mathbf{x}, z)$ vary linearly in z; however the transverse displacement w_z (displacement according to z) depends only

2. By writing the variables in bold, it indicates that they represent a nth order tensor. Otherwise, the variables are scalar.

on **x**. The transverse strain along z is assumed to be zero (no variation along the thickness). According to the plane stress hypothesis, the associated out-of-plane stress is negligible compared to the other components of the stress tensor. For any point P corresponds a point M

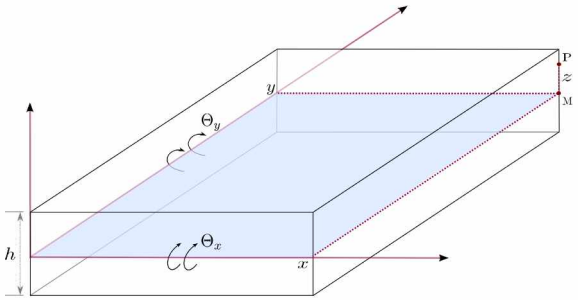

Figure 1: Illustration of a plate structure.

of coordinates $(\mathbf{x}, 0)$ belonging to the reference plane ($z = 0$) as illustrated in Fig.1. The displacement field $\mathbf{u}(\mathbf{x}, 0)$ of M is referred to the generalized displacement $\mathbf{U}(\mathbf{x})$ and expressed as follows:

$$\mathbf{u}(\mathbf{x},0) = \begin{bmatrix} u_x(\mathbf{x},0) \\ v_y(\mathbf{x},0) \\ w_z(\mathbf{x},0) \end{bmatrix} = \begin{bmatrix} U_x(\mathbf{x}) \\ V_y(\mathbf{x}) \\ W_z(\mathbf{x}) \end{bmatrix} = \mathbf{U}(\mathbf{x}) \tag{1}$$

where u_x, v_y and w_z are respectively the representative variables of the displacements according to x, y and z in the 3D plate. On the other hand, U_x, V_y and W_z are the generalized displacements respectively over x, y and z. In addition, the plane cross-sectional assumption implies the introduction of a rotation vector $\mathbf{\Theta}(\mathbf{x})$. Therefore, the displacement field $\mathbf{u}(\mathbf{x}, z)$ at point P is:

$$\mathbf{u}(\mathbf{x},z) = \begin{bmatrix} u_x(\mathbf{x},z) \\ v_y(\mathbf{x},z) \\ w_z(\mathbf{x},z) \end{bmatrix} = \begin{bmatrix} U_x(\mathbf{x}) \\ V_y(\mathbf{x}) \\ W_z(\mathbf{x}) \end{bmatrix} + z \underbrace{\begin{bmatrix} 0 & 1 & 0 \\ -1 & 0 & 0 \\ 0 & 0 & 0 \end{bmatrix}}_{\mathbf{R}} \begin{bmatrix} \Theta_x(\mathbf{x}) \\ \Theta_y(\mathbf{x}) \\ 0 \end{bmatrix} \tag{2}$$

Thus,

$$\mathbf{u}(\mathbf{x},z) = \mathbf{U}(\mathbf{x}) + z\mathbf{R}\mathbf{\Theta}(\mathbf{x}) \tag{3}$$

The strain field $\boldsymbol{\epsilon}$ derives from the displacement field $\mathbf{u}$. Taking into account the small strain hypothesis, $\boldsymbol{\epsilon}$ is written as:

$$\boldsymbol{\epsilon}(\mathbf{x},z) = \frac{1}{2}\left(\nabla\mathbf{u}(\mathbf{x},z) + \nabla^T\mathbf{u}(\mathbf{x},z)\right) \tag{4}$$

where ∇ is the gradient operator and $(\bullet)^T$ denotes the transpose.

In order to distinguish the different strain components of the plate (i.e. membrane, bending and shear), specific notations are used such as:

$$\mathbf{e} = \begin{bmatrix} e_x = U_{x,x} \\ e_y = V_{y,y} \\ 2e_{xy} = U_{x,y} + V_{y,x} \end{bmatrix}, \ \boldsymbol{\kappa} = \begin{bmatrix} \kappa_x = \Theta_{y,x} \\ \kappa_y = -\Theta_{x,y} \\ 2\kappa_{xy} = \Theta_{y,y} - \Theta_{x,x} \end{bmatrix}, \ \boldsymbol{\gamma} = \begin{bmatrix} \gamma_x = W_{z,x} + \Theta_y \\ \gamma_y = W_{z,y} - \Theta_x \end{bmatrix} \tag{5}$$

where $(\bullet)_{,a}$ denotes the spatial derivative of $\bullet$ with respect to coordinate $a \in \{x, y, z\}$. Therefore, the strain tensor (4) can be formulated

in vector form according to the Voigt's notation as follows:

$$\boldsymbol{\epsilon} = \begin{bmatrix} \mathbf{e} + z\boldsymbol{\kappa} \\ \boldsymbol{\gamma} \end{bmatrix} = \begin{bmatrix} e_x + z\kappa_x \\ e_y + z\kappa_y \\ 2e_{xy} + 2z\kappa_{xy} \\ \gamma_x \\ \gamma_y \end{bmatrix} \tag{6}$$

2.2. Principle of virtual works

Let us assume an arbitrary finite element plate e of surface Ω_e. The elementary internal virtual work W^e_{int} is written according to the variations of the virtual strains $\boldsymbol{\epsilon}^*$ where the upper index $(\bullet)^*$ is used to designate a virtual variable. Thus:

$$W^e_{int}(t) = \int_{\Omega_e} \int_{-\frac{h}{2}}^{\frac{h}{2}} \delta\boldsymbol{\epsilon}^{*T}(\mathbf{x}, z, t)\boldsymbol{\sigma}(\mathbf{x}, z, t) dz d\Omega_e \tag{7}$$

where t is the pseudo-time and $\boldsymbol{\sigma}$ is the stress vector composed of a plane part $\boldsymbol{\mathcal{S}}_p$ and a distortion part $\boldsymbol{\mathcal{S}}_z$ such as:

$$\boldsymbol{\sigma} = [\underbrace{\sigma_{xx} \;\; \sigma_{yy} \;\; \sigma_{xy}}_{\boldsymbol{\mathcal{S}}_p^T} \; \underbrace{\sigma_{xz} \;\; \sigma_{yz}}_{\boldsymbol{\mathcal{S}}_z^T}]^T \tag{8}$$

Then, by introducing the expression (6) of the strains $\boldsymbol{\epsilon}$ in (7) and by integrating along the thickness h, we get the following formula:

$$W^e_{int}(t) = \int_{\Omega_e} \delta\boldsymbol{\varepsilon}^{*T}(\mathbf{x}, t)\mathbf{F}(\mathbf{x}, t) d\Omega_e \tag{9}$$

with $\boldsymbol{\varepsilon}^*$ the plate generalized strains [3] such that $\boldsymbol{\varepsilon}^{*T} = [\mathbf{e}^* \;\; \boldsymbol{\kappa}^* \;\; \boldsymbol{\gamma}^*]$ (see Eq. (5)) and $\mathbf{F} = [\mathbf{N} \;\; \mathbf{M} \;\; \mathbf{T}]^T$ the plate generalized forces defined as follows:

$$\mathbf{N} = \int_{\frac{-h}{2}}^{\frac{h}{2}} \boldsymbol{\mathcal{S}}_p dz \;,\; \mathbf{M} = \int_{\frac{-h}{2}}^{\frac{h}{2}} z\boldsymbol{\mathcal{S}}_p dz \;,\; \mathbf{T} = \int_{\frac{-h}{2}}^{\frac{h}{2}} \boldsymbol{\mathcal{S}}_z dz \tag{10}$$

For the sake of conciseness, spatial and pseudo-time coordinates $\mathbf{x}$, z and t are omitted in the following.

2.3. Generalized constitutive laws

From a material point of view, we consider a plane stress elastic isotropic constitutive law. The three-dimensional constitutive law can be written as follows:

$$\boldsymbol{\sigma} = \mathbf{C}\boldsymbol{\epsilon} \tag{11}$$

with $\mathbf{C}$ the local stiffness matrix combining plane stresses and transverse distortion. For a homogeneous isotropic linear elastic behavior, $\mathbf{C}$ takes the following form:

$$\mathbf{C} = \frac{E}{1-\nu^2} \begin{bmatrix} 1 & \nu & 0 & 0 & 0 \\ \nu & 1 & 0 & 0 & 0 \\ 0 & 0 & \frac{1-\nu}{2} & 0 & 0 \\ 0 & 0 & 0 & \frac{k(1-\nu)}{2} & 0 \\ 0 & 0 & 0 & 0 & \frac{k(1-\nu)}{2} \end{bmatrix} \tag{12}$$

with k the transverse shear correction factor, E the Young's modulus and ν the Poisson's ratio. Furthermore, the matrix $\mathbf{C}$ can be put in the following simplified form:

$$\mathbf{C} = \begin{bmatrix} \mathbf{H} & 0 \\ 0 & \mathbf{H}_{\boldsymbol{\gamma}} \end{bmatrix} \tag{13}$$

3. It is important to note the difference between the strain field $\boldsymbol{\epsilon}$ expressed in three dimensions and the generalized deformation field $\boldsymbol{\varepsilon}$ having 8 components ($\boldsymbol{\epsilon} \neq \boldsymbol{\varepsilon}$).

with:

$$\mathbf{H} = \frac{E}{1-\nu^2}\begin{bmatrix} 1 & \nu & 0 \\ \nu & 1 & 0 \\ 0 & 0 & \frac{1-\nu}{2} \end{bmatrix} \ , \ \mathbf{H}_{\boldsymbol{\gamma}} = \frac{E}{1-\nu^2}\begin{bmatrix} \frac{k(1-\nu)}{2} & 0 \\ 0 & \frac{k(1-\nu)}{2} \end{bmatrix} \tag{14}$$

Therefore, the equation (11) can be written using (6), (8) and (13) as:

$$\boldsymbol{\sigma} = \begin{bmatrix} \boldsymbol{\mathcal{S}}_p \\ \boldsymbol{\mathcal{S}}_z \end{bmatrix} = \begin{bmatrix} \mathbf{H}(\mathbf{e} + z\boldsymbol{\kappa}) \\ \mathbf{H}_{\boldsymbol{\gamma}}\boldsymbol{\gamma} \end{bmatrix} \tag{15}$$

In order to obtain a generalized form of the plate behavior, the generalized force equations (10) are developed according to the material behavior law (15). Please see AppendixA for details. Therefore, the plate generalized behavior can be written as follows:

$$\begin{bmatrix} \mathbf{N} \\ \mathbf{M} \\ \mathbf{T} \end{bmatrix} = \begin{bmatrix} \mathbf{H}_m & \mathbf{H}_{mf} & \mathbf{0} \\ \mathbf{H}_{mf} & \mathbf{H}_f & \mathbf{0} \\ \mathbf{0} & \mathbf{0} & \mathbf{H}_{ct} \end{bmatrix} \begin{bmatrix} \mathbf{e} \\ \boldsymbol{\kappa} \\ \boldsymbol{\gamma} \end{bmatrix} \Leftrightarrow \mathbf{F} = \mathbf{D}\boldsymbol{\varepsilon} \tag{16}$$

with $\mathbf{D}$ the stiffness matrix of a plate element of thickness h. Lastly, the introduction of the generalized behavioral equation (16) into the expression of internal work (9) provides:

$$W_{int}^e = \int_{\Omega_e} \delta\boldsymbol{\varepsilon}^T \mathbf{D}\boldsymbol{\varepsilon} d\Omega_e \tag{17}$$

2.4. Finite Element discretization

Because computational cost is directly proportional to the number of integration points, engineers have a strong interest in using elements that require only one integration point per element. That is why the finite element chosen in this study is a triangular element with three nodes, referred hereafter as T3γ. Each node i has six degrees of freedom representing the three generalized displacements (U_{xi}, V_{yi} and W_{zi}), the two independent rotations (Θ_{xi} and Θ_{yi}) and the out-of-plane rotation (Θ_{zi}). The out-of-plane rotation has not been particularly explored since the study of torsion has not been covered in this paper but the corresponding degree of freedom is left in the formulation for compatibility reasons. However, since the out-of-plane rotation does not correspond to any stiffness, it is necessary to be careful in the numerical computation of the system of equations in order to avoid rank deficiencies. The six independent generalized components are expressed by the same linear interpolation functions [11].

$$\begin{array}{lll} U_x = \sum_i N_i U_{xi} & V_y = \sum_i N_i V_{yi} & W_z = \sum_i N_i W_{zi} \\ \Theta_x = \sum_i N_i \Theta_{xi} & \Theta_y = \sum_i N_i \Theta_{yi} & \Theta_z = \sum_i N_i \Theta_{zi} \end{array} \tag{18}$$

where N_i is the interpolation function corresponding to node i:

$$N_i(\mathbf{x}) = 1 - \frac{(\mathbf{x}^i - \mathbf{x}) \cdot \mathbf{n}^i}{h^i} \tag{19}$$

$\mathbf{n}^i$ is the normal vector to the opposite side of node i (directed, in our case, towards the inside of the triangular element) and h^i is the height associated with the node i. The assembly of these six equations (18) results in:

$$\mathbf{d} = \mathbf{N}\mathbf{d}_e \ \text{ such that } \ \mathbf{d} = \begin{bmatrix} U_x & V_y & W_z & \Theta_x & \Theta_y & \Theta_z \end{bmatrix}^T \tag{20}$$

with $\mathbf{N}$ the matrix of the interpolation functions associated with the six generalized displacement fields $\mathbf{d}$, and $\mathbf{d}_e$ the elementary vector of the 18 nodal degrees of freedom. Thus, the generalized displacement fields (20) can be differentiated to obtain the generalized strain fields as follows:

$$\boldsymbol{\varepsilon} = \mathbf{B}\mathbf{d}_e \tag{21}$$

with **B** the matrix of the first derivatives of the interpolation functions associated with the eight components of the generalized strain fields ε. By combining equations (21) and (17), we end up with the following expression:

$$W_{int}^{e} = \delta \mathbf{d}_e^T \left(\int_{\Omega_e} \mathbf{B}^T \mathbf{D} \mathbf{B} d\Omega_e \right) \mathbf{d}_e \tag{22}$$

According to equation (22), the elementary stiffness matrix of a plate element can be deduced and written as:

$$\mathbf{K}_e = \int_{\Omega_e} \mathbf{B}^T \mathbf{D} \mathbf{B} d\Omega_e \tag{23}$$

2.5. Shear locking

Shear locking is a numerical phenomenon which occurs with the MRP theory when the plate tends to be thin. This locking results in an overestimation of the bending stiffness. Several methods have been proposed in the literature to avoid this locking problem. To overcome this drawback, one can mention (i) the *uniform reduced integration*, where the bending and shear terms are both integrated with the same rule which is of a lower order than the required one [12]; (ii) *selective reduced integration*, where only the integration rule order of the shear terms is reduced [13]; (iii) the *mixed variational formulation*, which is capable of reducing the influence of shear energy. However, the resulting formulations are complex and computationally expensive [14]. Finally, (iv) the *Assumed Transverse Shear strain Field*, [15] which is used in this work since it avoids the problems raised by the reduced integration methods such as the development of strong distortions or Hourglass phenomena, and avoids the complexity of the mixed formulations. The spatial variation of the distortion

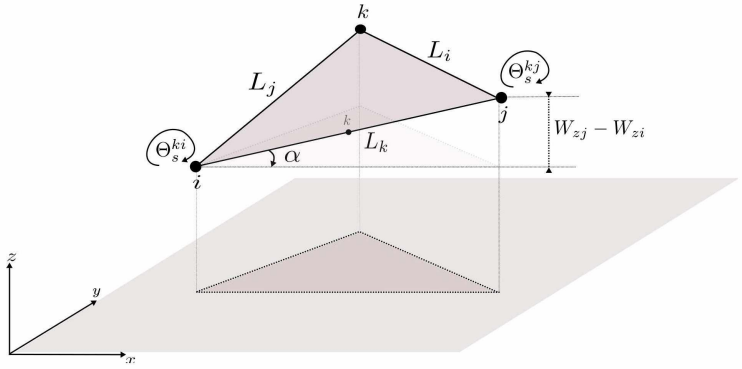

Figure 2: Simplified illustration of shear distortion.

is assumed to be linear with a constant tangential component on each side. The element compatibility is imposed in the middle of all three sides only in the tangential direction. The values of the tangential component γ_s^k of the transverse distortion along the side ij in Fig.2 can be calculated directly as follows:

$$\gamma_s^k = \underbrace{\frac{W_{zj} - W_{zi}}{L_k}}_{\sin\alpha, \text{ see Fig.2}} + \frac{1}{2}(\Theta_s^{ki} + \Theta_s^{kj}) \tag{24}$$

where Θ_s^{ki} and Θ_s^{kj} are the projected values of the rotations on the tangent of the side ij such that :

$$\Theta_s^{ki} = \Theta_x^i \cos\Omega_k + \Theta_y^i \sin\Omega_k \tag{25}$$

where Ω_k represents the angle of the side ij with respect to the horizontal axis of the local system of axes. This procedure allows to determine the interpolation functions associated with the transverse strains which leads to a shear locking free element. These functions

take the following forms:

$$\begin{bmatrix}\gamma_x\\ \gamma_y\end{bmatrix} = \mathbf{m}_1\mathbf{m}_2 \begin{bmatrix}\Theta_{yi}\\ -\Theta_{xi}\\ W_{zi}\\ \Theta_{yj}\\ -\Theta_{xj}\\ W_{zj}\\ \Theta_{yk}\\ -\Theta_{xk}\\ W_{zk}\end{bmatrix} \tag{26}$$

with:

$$\mathbf{m}_1 = \begin{bmatrix} 1-t & Qt & -\frac{S_j}{S_k}Qt \\ -\frac{C_k}{S_k} - \frac{1}{QS_j}s + \frac{C_k}{S_k}t & \frac{1}{S_j}s - \frac{C_k}{S_k}Qt & \frac{1}{S_k} - \frac{1}{S_k}s + \frac{C_kS_j}{S_k^2}Qt \end{bmatrix} \tag{27}$$

and:

$$\mathbf{m}_2 = \begin{bmatrix} \frac{1}{2} & 0 & -\frac{1}{L_i} & \frac{1}{2} & 0 & \frac{1}{L_i} & 0 & 0 & 0 \\ 0 & 0 & 0 & \frac{C_j}{2} & \frac{S_j}{2} & -\frac{1}{L_j} & \frac{C_j}{2} & \frac{S_j}{2} & \frac{1}{L_j} \\ \frac{C_k}{2} & \frac{S_k}{2} & \frac{1}{L_k} & 0 & 0 & 0 & \frac{C_k}{2} & \frac{S_k}{2} & -\frac{1}{L_k} \end{bmatrix} \tag{28}$$

and:

$$Q = \frac{1}{C_j - \frac{S_j}{S_k}C_k} \;\; ; \;\; C_l = \cos\Omega_l \;\; ; \;\; S_l = \sin\Omega_l \;\; ; \;\; l = \{i,j,k\} \tag{29}$$

where $\Omega_l = 0$ for $l = i$ as a result of changing the system of physical axes of the finite element ijk to the system of orthonormal axes of origin i. The variables s and t are the coordinates in the system of reference axes [4].

3. Enhanced plate model

3.1. Kinematic enhancement

The kinematic enhancement-based method using discontinuities has been proven as efficient to describe failure. Several enhanced models have been developed in literature [8, 17–19]. The kinematic enhancement is done within the framework of the generalized approach. In other words, the discontinuity variables are generalized ones. The idea is to introduce two discontinuity fields per element:

— $\overline{\overline{\mathbf{U}}}_e$: displacement discontinuity in the membrane;

— $\overline{\overline{\mathbf{\Theta}}}_e$: rotational discontinuity for bending.

The elementary discontinuity [5] vector $\overline{\overline{\mathbf{d}}}_e = [\overline{\overline{\mathbf{U}}}_e \;\; \overline{\overline{\mathbf{\Theta}}}_e]^T$ is represented by a thick black line designated Γ_d in Fig.3. The discontinuity line is generally inclined by an angle α with respect to the vertical axis and having $\mathbf{n} = [\cos\alpha \;\; \sin\alpha]^T$ as a normal vector. The line Γ_d divides the element into two domains: Ω_e^+ and Ω_e^-, see Fig.3. Each of the two discontinuity fields has two components, according to x and y as follows:

$$\overline{\overline{\mathbf{U}}}_e = \begin{cases} \overline{\overline{U}}_x = ||\overline{\overline{\mathbf{U}}}_e||\cos\alpha \\ \overline{\overline{V}}_y = ||\overline{\overline{\mathbf{U}}}_e||\sin\alpha \end{cases} \text{ and } \overline{\overline{\mathbf{\Theta}}}_e = \begin{cases} \overline{\overline{\Theta}}_x = ||\overline{\overline{\mathbf{\Theta}}}_e||\sin\alpha \\ \overline{\overline{\Theta}}_y = ||\overline{\overline{\mathbf{\Theta}}}_e||\cos\alpha \end{cases} \tag{30}$$

The two discontinuities are assumed to occur at the same position within the element. The opening of the membrane discontinuity is

4. Note that for this standard displacement formulation, membrane locking is not significant (i.e. the inability of the element to capture a state of pure bending problem [16]). Therefore, it does not raise any issues.

5. The variables highlighted with two upper bars refer to variables associated with discontinuities.

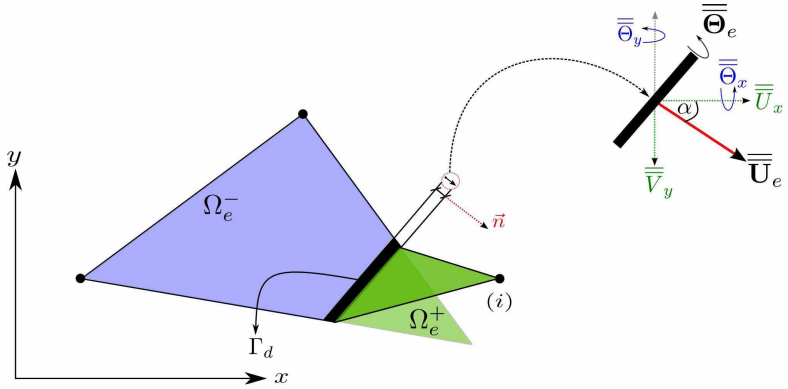

Figure 3: The components of the two discontinuities in the global system of axes.

assumed to be constant throughout the line Γ_d. This means that the two discontinuity lines are assumed to be parallel. In addition, it should be noted that only a mode I opening is considered in the model developed here. This means that in the local system of axes $(\mathbf{n}, \mathbf{t})$ corresponding to the discontinuity, see Fig.4, the tangent component $\overline{\overline{U}}_t$ representing the sliding between the two lips of the discontinuity is assumed to be setup to zero and thus, the sliding angle $\beta = \arctan\left(\frac{\overline{\overline{U}}_t}{\overline{\overline{U}}_n}\right)$ is zero too [6]. Therefore, one can write:

$$\overline{\overline{\mathbf{U}}}_e = \overline{\overline{U}}_n \mathbf{n} \tag{31}$$

The same consideration is made for the rotational discontinuity:

$$\overline{\overline{\mathbf{\Theta}}}_e = \overline{\overline{\Theta}}_n \mathbf{n} \tag{32}$$

In the framework of the model proposed in this paper, crack continuity between elements is not taken into account. To do this, an

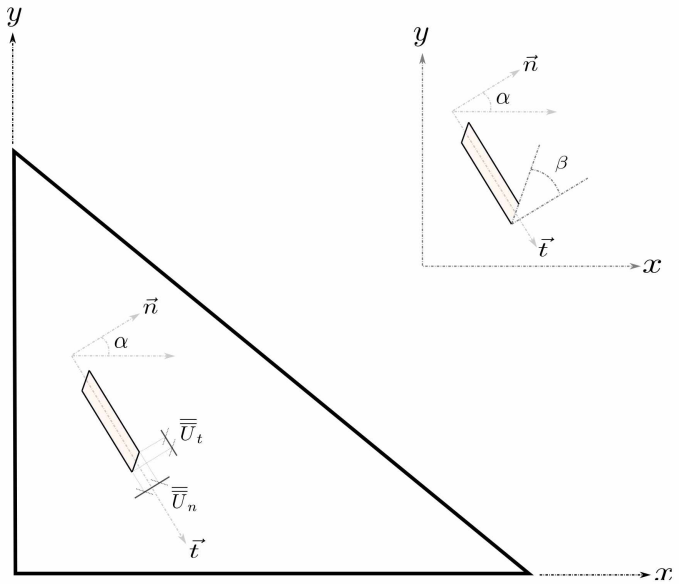

Figure 4: Representation of the general case of a membrane discontinuity.

additional compatibility condition must be introduced and global/local crack tracking algorithms should be used in order to ensure the continuity of the crack-path in particular under complex cracking conditions involving curved cracks [20].

6. It should be noted that the extension to mode II opening is not a difficulty. This can be done by considering the tangent component $\overline{\overline{U}}_t$ of the discontinuity variable $\overline{\overline{\mathbf{U}}}_e$

The application of the enhancement to equation results in the following expression:

$$\begin{aligned}\mathbf{d}(\mathbf{x},t) &= \overline{\mathbf{d}}(\mathbf{x},t) + \overline{\overline{\mathbf{d}}}(\mathbf{x},t) \\ &= \mathbf{N}(\mathbf{x})\mathbf{d}_e(t) + \boldsymbol{\mathcal{M}}(\mathbf{x},\mathbf{x}_d)\overline{\overline{\mathbf{d}}}_e(t) \\ &= \mathbf{N}(\mathbf{x})\mathbf{d}_e(t) + [\boldsymbol{\varphi}(\mathbf{x}) + \boldsymbol{\mathcal{H}}(\mathbf{x}_d)]\,\overline{\overline{\mathbf{d}}}_e(t)\end{aligned} \tag{33}$$

with $\mathbf{x}_d$ the position of discontinuity line in the element, $\boldsymbol{\mathcal{H}}(\mathbf{x}_d)$ the Heaviside function at $\mathbf{x}_d$ and $\boldsymbol{\varphi}$ an appropriate function requires that the enhanced component of the displacement field to be equal to zero at the element nodes. Therefore, the generalized strain field becomes:

$$\begin{aligned}\boldsymbol{\varepsilon}(\mathbf{x},t) &= \overline{\boldsymbol{\varepsilon}}(\mathbf{x},t) + \boldsymbol{\nabla}\overline{\overline{\mathbf{d}}}(\mathbf{x},t) \\ &= \mathbf{B}(\mathbf{x})\mathbf{d}_e(t) + \mathbf{G}_r(\mathbf{x},\mathbf{x}_d)\overline{\overline{\mathbf{d}}}_e(t) \\ &= \underbrace{\mathbf{B}(\mathbf{x})\mathbf{d}_e(t) + \overline{\mathbf{G}}_r(\mathbf{x},\mathbf{x}_d)\overline{\overline{\mathbf{d}}}_e(t)}_{\tilde{\boldsymbol{\varepsilon}}(\mathbf{x},t)} + \underbrace{\boldsymbol{\delta}(\mathbf{x}_d)\overline{\overline{\mathbf{d}}}_e(t)}_{\overline{\overline{\boldsymbol{\varepsilon}}}(\mathbf{x}_d,t)}\end{aligned} \tag{34}$$

with $\boldsymbol{\delta}(\mathbf{x}_d)$ the Dirac function centered at $\mathbf{x}_d$ and $\overline{\mathbf{G}}_r(\mathbf{x},\mathbf{x}_d) = \frac{\partial \boldsymbol{\varphi}(\mathbf{x},\mathbf{x}_d)}{\partial \mathbf{x}}$ the compatibility operators associated with real enhancement variables such that:

$$\overline{\mathbf{G}}_r(\mathbf{x},\mathbf{x}_d) = \begin{bmatrix} \overline{\mathbf{G}}_{rm}(\mathbf{x}) & \mathbf{0} \\ \mathbf{0} & \overline{\mathbf{G}}_{r\kappa}(\mathbf{x}) \\ \mathbf{0} & \mathbf{R}\boldsymbol{\mathcal{M}}_\theta(\mathbf{x},\mathbf{x}_d) \end{bmatrix} \tag{35}$$

where $\boldsymbol{\mathcal{M}}_\theta$ is the matrix of enhancement functions associated with the rotation discontinuity such that $\boldsymbol{\mathcal{M}}_\theta = \boldsymbol{\phi}_\theta(\mathbf{x}) + \boldsymbol{\mathcal{H}}_\theta(\mathbf{x}_d)$ and

$$\boldsymbol{\delta}(\mathbf{x}_d) = \begin{bmatrix} \boldsymbol{\delta}_m(\mathbf{x}_d) & \mathbf{0} \\ \mathbf{0} & \boldsymbol{\delta}_\kappa(\mathbf{x}_d) \\ \mathbf{0} & \mathbf{0} \end{bmatrix} \text{ with } \boldsymbol{\delta}_m = \boldsymbol{\delta}_\kappa = \begin{cases} \infty \;\text{ for }\; \mathbf{x} = \mathbf{x}_d \\ 0 \;\text{ otherwise} \end{cases} \tag{36}$$

Since linear triangles are considered, the strain field is constant within the element. Therefore, the discontinuity line can be set to any position within the element except that its direction is defined according to the principal direction (Rankine criterion). Indeed, the normal vector at the discontinuity line is parallel to the direction of the principal stress. Finally, we consider that the discontinuity line passes through the centre of gravity of the cracked element.

3.2. Variational formulation

The virtual strain field $\boldsymbol{\varepsilon}^*$ is written as a function of $\mathbf{d}_e^*$ and $\overline{\overline{\mathbf{d}}}_e^*$:

$$\boldsymbol{\varepsilon}^*(\mathbf{x},t) = \mathbf{B}(\mathbf{x})\mathbf{d}_e^*(t) + \mathbf{G}_v(\mathbf{x},\mathbf{x}_d)\overline{\overline{\mathbf{d}}}_e^*(t) \tag{37a}$$

$$= \mathbf{B}(\mathbf{x})\mathbf{d}_e^*(t) + \overline{\mathbf{G}}_v(\mathbf{x})\overline{\overline{\mathbf{d}}}_e^*(t) + \boldsymbol{\delta}(\mathbf{x}_d)\overline{\overline{\mathbf{d}}}_e^*(t) \tag{37b}$$

The virtual discontinuity variable $\overline{\overline{\mathbf{d}}}_e^*$ is interpolated using the enhancement functions $\mathbf{G}_v$ named the equilibrium operators. In general, $\mathbf{G}_r$ and $\mathbf{G}_v$ are not necessarily the same. Each of them can be determined according to specific conditions, as shown in section (3.4).

Remembering equation (9) in which (37a) is introduced, the following expression can be derived:

$$W_{int}^e(t) = \delta\mathbf{d}_e^{*T}(t)\mathbf{F}_{int,B}^e(t) + \delta\overline{\overline{\mathbf{d}}}_e^{*T}(t)\mathbf{F}_{int,G}^e(t) \tag{38}$$

where:

$$\mathbf{F}^e_{int,B}(t) = \int_{\Omega_e} \mathbf{B}^T(\mathbf{x})\mathbf{F}(\mathbf{x},t)d\Omega_e \tag{39}$$

$$\mathbf{F}^e_{int,G}(t) = \int_{\Omega_e} \mathbf{G}^T_v(\mathbf{x})\mathbf{F}(\mathbf{x},t)d\Omega_e \tag{40}$$

After determining the expression of the elementary internal work, the principle of virtual works is written as:

$$\begin{aligned}
&\sum_e^n \{W^e_{int}(t) - W^e_{ext}(t)\} = 0 \\
&\sum_e^n \delta\mathbf{d}^{*T}_e(t)(\mathbf{F}^e_{int,B}(t) - \mathbf{F}^e_{ext}(t)) + \sum_e^{\overline{\overline{n}}} \delta\overline{\overline{\mathbf{d}}}^{*T}_e(t)\mathbf{F}^e_{int,G}(t) = 0 \\
&\delta\mathbf{d}^{*T}_{str}(t)(\mathbf{F}^{str}_{int,B}(t) - \mathbf{F}^{str}_{ext}(t)) + \sum_e^{\overline{\overline{n}}} \delta\overline{\overline{\mathbf{d}}}^{*T}_e(t)\mathbf{F}^e_{int,G}(t) = 0
\end{aligned} \tag{41}$$

with

$$\mathbf{d}_{str} = \begin{bmatrix} U_{x1} & V_{y1} & W_{z1} & \dots & \Theta_{xm} & \Theta_{ym} & \Theta_{zm} \end{bmatrix}^T$$

with m the total number of nodes, n the total number of plate finite elements and $\overline{\overline{n}}$ the number of plate elements with, at least, one active discontinuity. The activation of the discontinuity is assumed to be defined by a Rankine's failure criterion. In addition, the equilibrium must be fulfilled for all virtual displacements $\delta\mathbf{d}^*_{str}$ as well as for all elementary virtual jumps $\delta\overline{\overline{\mathbf{d}}}^*_e$. Therefore, the following system is obtained:

$$\mathbf{F}^{str}_{int,B}(t) - \mathbf{F}^{str}_{ext}(t) = 0 \tag{42a}$$

$$\forall e \in \{1,2,\dots,\overline{\overline{n}}\} \qquad \mathbf{F}^e_{int,G}(t) = 0 \tag{42b}$$

The first equation of this system represents the structure equilibrium at a global level. The second equation represents the elementary equilibrium at local level. The development of the second equilibrium equation gives:

$$\begin{aligned}
\mathbf{F}^e_{int,G}(t) &= \int_{\Omega_e} \mathbf{G}^T_v(\mathbf{x})\mathbf{F}(\mathbf{x},t)d\Omega_e \\
&= \int_{\Omega_e} \left(\overline{\mathbf{G}}^T_v(\mathbf{x}) + \boldsymbol{\delta}^T(\mathbf{x}_d)\right)\mathbf{F}(\mathbf{x},t)d\Omega_e = 0
\end{aligned} \tag{43}$$

Therefore, we end up with the following equation:

$$\int_{\Omega_e} \overline{\mathbf{G}}^T_v(\mathbf{x})\mathbf{F}(\mathbf{x},t)d\Omega_e = -\int_{\Omega_e} \boldsymbol{\delta}^T(\mathbf{x}_d)\mathbf{F}(\mathbf{x},t)d\Omega_e \tag{44}$$

where $\boldsymbol{\delta}^T(\mathbf{x}_d)$ is given in equation (36) and:

$$\overline{\mathbf{G}}^T_v(\mathbf{x},\mathbf{x}_d) = \begin{bmatrix} \overline{\mathbf{G}}_{vm}(\mathbf{x}) & \mathbf{0} & \mathbf{0} \\ \mathbf{0} & \overline{\mathbf{G}}_{v\kappa}(\mathbf{x}) & \mathbf{R}\boldsymbol{\mathcal{M}}_\theta(\mathbf{x},\mathbf{x}_d) \end{bmatrix} \tag{45}$$

The following system of equations is obtained [7]:

$$\int_{\Omega_e} \overline{\mathbf{G}}^T_{vm}(\mathbf{x})\mathbf{N}(\mathbf{x},t)d\Omega_e = -\int_{\Gamma_d} \mathbf{N}(\mathbf{x},t)d\Gamma_d = \mathbf{N}(\mathbf{x}_d,t)l_{\Gamma_d}$$

7. Equations (46) were obtained by knowing the following Dirac function property:

$$\int_{\Omega_e} \boldsymbol{\delta}^T(\mathbf{x}_d)\mathbf{F}(\mathbf{x},t)d\Omega_e = \int_{\Gamma_d} \mathbf{F}(\mathbf{x},t)d\Gamma_d = \mathbf{F}(\mathbf{x}_d,t)l_{\Gamma_d}$$

$$\int_{\Omega_e} \overline{\mathbf{G}}_{vk}^T(\mathbf{x})\mathbf{M}(\mathbf{x},t)\Omega_e + \int_{\Omega_e} \left[\mathbf{R}\boldsymbol{\mathcal{M}}_\theta(\mathbf{x},\mathbf{x}_d)\right]^T \mathbf{T}(\mathbf{x},t)d\Omega_e = -\int_{\Gamma_d} \mathbf{M}(\mathbf{x},t)d\Gamma_d = \mathbf{M}(\mathbf{x}_d,t)l_{\Gamma_d} \tag{46}$$

3.3. Generalized cohesive laws

The material behavior at the level of the membrane and rotation discontinuities needs now to be defined. For this purpose, a generalized traction separation law is considered. For quasi-brittle materials, discrete cracking can be modeled by either a damage model or a plasticity model. For more details about these strategies, see [21]. In this work, a cohesive damage-based model is chosen. Discontinuity initiation is assumed to be defined by a Rankine's failure criterion. In addition, discontinuity is assumed to occur along a localized surface oriented perpendicularly to the direction of the maximum principal stress. The discontinuity activation and evolution can be described either by neglecting shear stresses or by taking into account the two stress components (axial and shear) in the definition of the failure surface. For both membrane and bending components we assume a linear elastic model in the bulk. Nevertheless, a cohesive model takes control at the discontinuity level. For the membrane component, the membrane discontinuity is likely to develop only in tension beyond a certain stress threshold. This choice is made in order to distinguish between the behaviour of concrete in tension and compression. On the other hand, for the bending component, the rotational discontinuity can develop either in tension or in compression since a symmetrical behavior is considered to represent the concrete cross-section.

The failure criterion ϕ_m for membrane and ϕ_f for bending are computed by comparing the values of the normal components with the ultimate stress values (N_u and M_u) allowed before the discontinuities are initiated:

$$\phi_m(t) = N_n(t) - N_u(t) \leq 0 \;\text{ and }\; \phi_f(t) = |M_n(t)| - M_u(t) \leq 0 \tag{47}$$

where N_n and M_n are the normal components of the generalized membrane and bending forces in the discontinuity system of axes. N_u and M_u represent their limit values which evolve according to the softening cohesive laws. The cohesive models take standard exponential forms:

$$N = N_u \exp(-\frac{N_u}{G_m}\overline{\overline{U}}_n) \;\text{ and }\; M = M_u \exp(-\frac{M_u}{G_f}\overline{\overline{\Theta}}_n) \tag{48}$$

with G_m and G_f the fracture energies in membrane and bending respectively. For more details about the thermodynamic framework of this cohesive damage model, readers are invited to refer to paper [21].

3.4. Enhancement operators

3.4.1. Compatibility operators

Two conditions must be fulfilled in order to determine these operators [22].

First, the presence of discontinuity must not affect nodal compatibility between the elements. The following equations are derived from this condition:

$$\boldsymbol{\mathcal{M}}(\mathbf{x},\mathbf{x}_d) = \boldsymbol{\mathcal{H}}(\mathbf{x}_d) + \boldsymbol{\varphi}(\mathbf{x}) = \boldsymbol{\mathcal{H}}(\mathbf{x}_d) - \sum_{i\in\Omega^+} \mathbf{N}_i(\mathbf{x}) \tag{49}$$

Therefore:

$$\overline{\mathbf{G}}_r(\mathbf{x}) = -\sum_{i\in\Omega^+} \mathbf{B}_i(\mathbf{x}) \tag{50}$$

Second, the cracked element must be able to reproduce a zero strain state when the discontinuities are fully opened. In this case, at the pseudo time $t = t_f$, the kinematic relationships between the discontinuities can be obtained by writing the displacement at node i belonging Ω_e^+ in Fig.3 as follows:

$$\mathbf{d}_i^{hinge}(t_f) = \mathbf{d}_i^{rigid}(t_f) + \mathbf{D}_i^{hinge}\overline{\overline{\mathbf{d}}}_e(t_f) \tag{51}$$

with:

$$\mathbf{D}_i^{hinge} = \begin{bmatrix} 1 & 0 \\ 0 & \mathbf{x}^i - \mathbf{x}_{\Gamma_d} \\ 0 & 1 \\ 0 & 0 \end{bmatrix} \tag{52}$$

For the other nodes (j) and (k) of the element belonging to Ω_e^-, their nodal displacement vectors in case of a zero strain state $\mathbf{d}_j^{hinge}(t_f)$ and $\mathbf{d}_k^{hinge}(t_f)$ are equal to those of their rigid states $\mathbf{d}_j^{rigid}(t_f)$ and $\mathbf{d}_k^{rigid}(t_f)$ such that:

$$\mathbf{d}_j^{hinge}(t_f) = \mathbf{d}_j^{rigid}(t_f) \;\text{ and }\; \mathbf{d}_k^{hinge}(t_f) = \mathbf{d}_k^{rigid}(t_f) \tag{53}$$

By assembling the three nodal displacement vectors, the elementary displacement vector is obtained as follows:

$$\mathbf{d}_e^{hinge}(t_f) = \mathbf{d}_e^{rigid}(t_f) + \mathbf{D}_e^{hinge}\overline{\overline{\mathbf{d}}}_e(t_f) \tag{54}$$

with:

$$\mathbf{D}_e^{hinge} = \begin{bmatrix} \mathbf{D}_i^{hinge} \\ 0 \\ 0 \end{bmatrix} \tag{55}$$

The regular part $\tilde{\boldsymbol{\varepsilon}}$ of the enhanced strain $\boldsymbol{\varepsilon}$ in (34) must be cancelled in case of a zero strain state. This results in:

$$0 = \mathbf{B}(\mathbf{x})\mathbf{D}_e^{hinge}\overline{\overline{\mathbf{d}}}_e(t_f) + \overline{\mathbf{G}}_r(\mathbf{x})\overline{\overline{\mathbf{d}}}_e(t_f) \tag{56}$$

with $\mathbf{B}(\mathbf{x})\mathbf{d}_e^{rigid}(t_f) = 0$. Therefore, the introduction of (55) in equation (56) gives:

$$\overline{\mathbf{G}}_r(\mathbf{x}) = -\mathbf{B}_i(\mathbf{x})\mathbf{D}_i^{hinge} \tag{57}$$

Knowing that,

$$\overline{\mathbf{G}}_r(\mathbf{x}) = \begin{bmatrix} \overline{\mathbf{G}}_{rm}(\mathbf{x}) \\ \overline{\mathbf{G}}_{r\kappa}(\mathbf{x}) \\ \overline{\mathbf{G}}_{r\gamma}(\mathbf{x}) \end{bmatrix} = \begin{bmatrix} \overline{\mathbf{G}}_{rm\overline{\overline{u}}}(\mathbf{x}) & 0 \\ 0 & \overline{\mathbf{G}}_{r\kappa\overline{\overline{\theta}}}(\mathbf{x}) \\ 0 & \overline{\mathbf{G}}_{r\gamma\overline{\overline{\theta}}}(\mathbf{x}) \end{bmatrix}, \tag{58}$$

we obtain:

$$\begin{aligned} \overline{\mathbf{G}}_{rm\overline{\overline{u}}}(\mathbf{x}) &= -\mathbf{B}_{m\mathbf{u}i}(\mathbf{x}) \\ \overline{\mathbf{G}}_{r\kappa\overline{\overline{\theta}}}(\mathbf{x}) &= -\mathbf{B}_{\kappa\boldsymbol{\theta}i}(\mathbf{x}) \\ \overline{\mathbf{G}}_{r\gamma\overline{\overline{\theta}}}(\mathbf{x}) &= -\mathbf{B}_{\gamma wi}(\mathbf{x})(\mathbf{x}^i - \mathbf{x}_{\Gamma_d}) - \mathbf{N}_{\theta i}(\mathbf{x}) \end{aligned} \tag{59}$$

For a three-node element T3γ which has linear shape functions (cf. equation (19)), the expressions of the compatibility operators can be deduced directly from the equation (58). Therefore, the functions associated with the membrane part and the bending part are:

$$\overline{\mathbf{G}}_{rm\overline{\overline{u}}}(\mathbf{x}) = \overline{\mathbf{G}}_{r\kappa\overline{\overline{\theta}}}(\mathbf{x}) = -\frac{1}{h^i}\begin{bmatrix} n_1^i & 0 \\ 0 & n_2^i \\ n_2^i & n_1^i \end{bmatrix} \tag{60}$$

with $\mathbf{n}^i = (n_1^i, n_2^i)$ the normal vector on the opposite side of the main node i and h^i the element height. The discontinuity line is assumed to be parallel to the opposite side of the main node. Thus, they have the same normal vector. Finally, regarding the enhancement functions $\overline{\mathbf{G}}_{r\gamma\bar{\bar{\theta}}}$ related to the shear strain $\boldsymbol{\gamma}$, we have :

$$\overline{\mathbf{G}}_{r\gamma\bar{\bar{\theta}}}(\mathbf{x}) = -\mathbf{B}_{\gamma wi}(\mathbf{x})(\mathbf{x}^i - \mathbf{x}_{\Gamma_d}) - \mathbf{N}_{\theta i}(\mathbf{x}) \tag{61}$$

Therefore, the choice of the enhancement functions $\overline{\mathbf{G}}_{r\gamma\bar{\bar{\theta}}}$ depends on the choice of the functions $\mathbf{B}_{\gamma wi}$ and $\mathbf{N}_{\boldsymbol{\theta} i}$ associated with the node i.

3.4.2. Equilibrium operators

The enhancement functions $\mathbf{G}_v$, also known as equilibrium operators, must verify the stress continuity between the continuous model and the cohesive model. In other words, they must satisfy equation (46). It is also necessary to check the patch test condition. An additional equation must be introduced in order to ensure the continuity of traction vectors through the discontinuity line. In other words, the normal cohesive forces $\mathbf{N}_d$ and bending cohesive forces $\mathbf{M}_d$ on the discontinuity line Γ_d are defined as a function of the normal force $\mathbf{N}$ and the bending moment $\mathbf{M}$ defined in the element Ω_e outside Γ_d. The weak form of these equations is written as:

$$-\int_{\Gamma_d} \mathbf{N}\mathbf{n} d\Gamma_d + \int_{\Gamma_d} \mathbf{N}_d d\Gamma_d = 0 \tag{62}$$

$$-\int_{\Gamma_d} \left[\mathbf{M}\mathbf{n} + (\mathbf{x} - \mathbf{x}_d)\mathbf{V}\mathbf{n}\right] d\Gamma_d + \int_{\Gamma_d} \left[\mathbf{M}_d + (\mathbf{x} - \mathbf{x}_d)\mathbf{V}_d\right] d\Gamma_d = 0 \tag{63}$$

However, according to [8], functions $\mathbf{G}_v$ are defined to allow the transition from an integration along the discontinuity line Γ_d to an integration over the element Ω_e. Therefore, taking into account this idea to express the first terms of equations (62) and (63) respectively allows us to write :

$$\int_{\Omega_e} \overline{\mathbf{G}}^T_{vm\bar{\bar{u}}}(\mathbf{x})\mathbf{N}(\mathbf{x}, t) d\Omega_e + \int_{\Gamma_d} \mathbf{N}_d d\Gamma_d = 0 \tag{64}$$

$$\begin{aligned}\int_{\Omega_e} \left[\overline{\mathbf{G}}^T_{v\kappa\bar{\bar{\theta}}}(\mathbf{x})\mathbf{M}(\mathbf{x}, t) + \overline{\mathbf{G}}^T_{v\gamma\bar{\bar{\theta}}}(\mathbf{x})\mathbf{V}(\mathbf{x}, t)\right] d\Omega_e \\ + \int_{\Gamma_d} \left[\mathbf{M}_d + (\mathbf{x} - \mathbf{x}_d)\mathbf{V}_d\right] d\Gamma_d = 0\end{aligned} \tag{65}$$

For $\mathbf{x} = \mathbf{x}_d$, we obtain $\int_{\Gamma_d} (\mathbf{x} - \mathbf{x}_d)\mathbf{V}_d d\Gamma_d = 0$. As a consequence, we find the same local equilibrium equations derived from the virtual work principle (46). By analogy between (64), (65) and (62), (63), one can deduce:

$$\int_{\Omega_e} \overline{\mathbf{G}}_{vm\bar{\bar{u}}}(\mathbf{x})\mathbf{N} d\Omega_e = -\int_{\Gamma_d} \mathbf{N}\mathbf{n}\, d\Gamma_d + l_{\Gamma_d} o(h_e^{p+1}) \tag{66}$$

$$\int_{\Omega_e} \overline{\mathbf{G}}_{v\kappa\bar{\bar{\theta}}}(\mathbf{x})\mathbf{M} d\Omega_e = -\int_{\Gamma_d} \mathbf{M}\mathbf{n}\, d\Gamma_d + l_{\Gamma_d} o(h_e^{p+1}) \tag{67}$$

$$\int_{\Omega_e} \overline{\mathbf{G}}_{v\gamma\bar{\bar{\theta}}}(\mathbf{x})\mathbf{V} d\Omega_e = -\int_{\Gamma_d} (\mathbf{x} - \mathbf{x}_d)\mathbf{V}\mathbf{n}\, d\Gamma_d + l_{\Gamma_d} o(h_e^{p+1}) \tag{68}$$

where l_{Γ_d} is the length of the discontinuity line, Γ_d and $o(h_e^{p+1})$ stands for higher order terms for $p \geq 0$. In [8], general expressions for $\overline{\mathbf{G}}^T_{vm\bar{\bar{u}}}$, $\overline{\mathbf{G}}^T_{v\kappa\bar{\bar{\theta}}}$ and $\overline{\mathbf{G}}^T_{v\gamma\bar{\bar{\theta}}}$ satisfying the equations (66), (67) and (67) have been determined. The proposed expressions depend on the interpolation functions order. In case of a T3γ element, the interpolation functions for the strain field are constant. A simple expression is proposed for the equilibrium operator in [23] in the context of a plane stress problem. Therefore, we can use these functions for both the membrane and the bending parts independently:

$$\overline{\mathbf{G}}_{vm} = \overline{\mathbf{G}}_{v\kappa} = -\frac{l_{\Gamma_d}}{S_{\Omega_e}} \begin{bmatrix} n_1 & 0 \\ 0 & n_2 \\ n_2 & n_1 \end{bmatrix} \tag{69}$$

with S_{Ω_e} the element surface and $\mathbf{n} = (n_1, n_2)$ the normal vector at the discontinuity line. Lastly, the patch test ensures the possibility of representing a constant stress state per element [24]. Indeed, in order to perform the patch test, the following condition (70) must be checked.

$$\begin{aligned} &\int_{\Omega_e} \mathbf{G}_{vm} d\Omega_e = 0, \text{ knowing that } \mathbf{G}_{vm} = \overline{\mathbf{G}}_{vm} + \boldsymbol{\delta}_m(\mathbf{x}_d), \\ \Rightarrow &\int_{\Omega_e} \overline{\mathbf{G}}_{vm} d\Omega_e = -\int_{\Omega_e} \boldsymbol{\delta}_m(\mathbf{x}_d) d\Omega_e = -l_{\Gamma_d} \begin{bmatrix} n_1 & 0 \\ 0 & n_2 \\ n_2 & n_1 \end{bmatrix} \end{aligned} \tag{70}$$

Therefore, the introduction of the equilibrium operator expression (69) in (70) allows us to easily fulfill the patch test.

4. Computational framework

4.1. Linearization procedure

The equilibrium equations of the system (42) are not generally linear. That is why, they must be linearized in order to be implemented. Let us assume that the variables of the problem are determined at pseudo-time t. The objective is to determine these variables at pseudo-time $t+1$. The residue associated with equation (42a) is defined as follows:

$$\begin{aligned} \mathbf{R}(\mathbf{d}_{str}, \overline{\overline{\mathbf{d}}}_1, \overline{\overline{\mathbf{d}}}_1, \ldots, \overline{\overline{\mathbf{d}}}_{\overline{\overline{n}}}) &= \mathbf{F}^{str}_{int,B}(t) - \mathbf{F}^{str}_{ext}(t) \\ &= \mathop{\mathrm{A}}_{e=1}^{n} \left\{ \mathbf{F}^{e}_{int,B}(t) - \mathbf{F}^{e}_{ext}(t) \right\} \end{aligned} \tag{71}$$

with,

$$\begin{cases} \dfrac{\partial \mathbf{R}}{\partial \mathbf{d}_{str}} = \mathop{\mathrm{A}}_{e=1}^{n} \left(\dfrac{\partial \mathbf{F}^{e}_{int,B}}{\partial \mathbf{d}_e} \right) \\ \dfrac{\partial \mathbf{R}}{\partial \overline{\overline{\mathbf{d}}}_e} = \dfrac{\partial \mathbf{F}^{e}_{int,B}}{\partial \overline{\overline{\mathbf{d}}}_e} \quad \forall e \in \{1, \ldots, \overline{\overline{n}}\} \end{cases} \tag{72}$$

The symbol A refers to the assembly operator. Then, the overall equilibrium of the structure is achieved iteratively using the index k according to a fixed point method. We end up with:

$$\begin{aligned} \mathbf{R}^{(k+1)}_{t+1} &= \mathbf{R}^{(k)}_{t+1} + \frac{\partial \mathbf{R}}{\partial \mathbf{d}_{str}} \cdot \Delta \mathbf{d}^{(k+1)}_{e,t+1} + \sum_{e=1}^{\overline{\overline{n}}} \frac{\partial \mathbf{R}}{\partial \overline{\overline{\mathbf{d}}}_e} \cdot \Delta \overline{\overline{\mathbf{d}}}^{(k+1)}_{e,t+1} \\ 0 &= \mathbf{R}^{(k)}_{t+1} + \mathop{\mathrm{A}}_{e=1}^{n} \mathbf{K}_{BB} \cdot \Delta \mathbf{d}^{(k+1)}_{e,t+1} + \sum_{e=1}^{\overline{\overline{n}}} \mathbf{K}_{BG} \cdot \Delta \overline{\overline{\mathbf{d}}}^{(k+1)}_{e,t+1} \end{aligned} \tag{73}$$

with $\mathbf{K}_{BB}$ and $\mathbf{K}_{BG}$ the stiffness matrices such that:

$$\mathbf{K}_{BB} = \frac{\partial \mathbf{F}^{e}_{int,B}}{\partial \mathbf{d}_e} = \int_{\Omega_e} \mathbf{B}^T(\mathbf{x}) \frac{\partial \mathbf{F}}{\partial \tilde{\boldsymbol{\varepsilon}}}(\mathbf{x}) \mathbf{B}(\mathbf{x}) d\Omega_e \tag{74}$$

$$\mathbf{K}_{BG} = \frac{\partial \mathbf{F}^{e}_{int,B}}{\partial \overline{\overline{\mathbf{d}}}_e} = \int_{\Omega_e} \mathbf{B}^T(\mathbf{x}) \frac{\partial \mathbf{F}}{\partial \tilde{\boldsymbol{\varepsilon}}}(\mathbf{x}) \overline{\mathbf{G}}_r(\mathbf{x}) d\Omega_e \tag{75}$$

Therefore, equation (73) can be reformulated into a matrix form as follows:

$$\mathop{\mathrm{A}}_{e=1}^{n} \begin{bmatrix} \mathbf{K}_{BB} & \mathbf{K}_{BG} \end{bmatrix}^{(k)}_{t+1} \begin{bmatrix} \Delta \mathbf{d}_e \\ \Delta \overline{\overline{\mathbf{d}}}_e \end{bmatrix}^{(k+1)}_{t+1} = -\mathop{\mathrm{A}}_{e=1}^{n} (\mathbf{F}^{e}_{int,B} - \mathbf{F}^{e}_{ext})^{(k)}_{t+1} \tag{76}$$

Similarly, equation (42b), qualified as local, is also linearized. This step is done at a constant displacement increment $\Delta\mathbf{d}_e$ at the pseudo-time step $t+1$ and at the iteration k:

$$\begin{aligned}\mathbf{F}_{int,G}^{e,(l+1)} &= \mathbf{F}_{int,G}^{e,(l)} + \frac{\partial \mathbf{F}_{int,G}^{e,(l)}}{\partial \mathbf{d}_e}\Delta\mathbf{d}_{e,t+1}^{(k)} + \frac{\partial \mathbf{F}_{int,G}^{e,(l)}}{\partial \overline{\overline{\mathbf{d}}}_e}\Delta\overline{\overline{\mathbf{d}}}_e^{(l+1)} \\ 0 &= \mathbf{F}_{int,G}^{e,(l)} + \mathbf{K}_{GB}^{(l)}\Delta\mathbf{d}_e^{(k)} + \mathbf{K}_{GG}^{(l)}\Delta\overline{\overline{\mathbf{d}}}_e^{(l+1)}\end{aligned} \tag{77}$$

such that:

$$\mathbf{F}_{int,G}^{e}(t) = \int_{\Omega_e} \overline{\mathbf{G}}_v^T(\mathbf{x})\mathbf{F}(\mathbf{x},t)d\Omega + \mathbf{F}(\mathbf{x}_d,t)l_{\Gamma_d} \tag{78}$$

with l_{Γ_d} the length of the discontinuity Γ_d and $\mathbf{F}(\mathbf{x}_d,t)$ the vector of cohesive forces. Therefore:

$$\mathbf{K}_{GB}(t) = \frac{\partial \mathbf{F}_{int,G}^{e}}{\partial \mathbf{d}_e}(t) = \int_{\Omega_e} \overline{\mathbf{G}}_v^T(\mathbf{x})\frac{\partial \mathbf{F}}{\partial \tilde{\boldsymbol{\varepsilon}}}(\mathbf{x},t)\mathbf{B}(\mathbf{x})d\Omega \tag{79}$$

$$\mathbf{K}_{GG}(t) = \frac{\partial \mathbf{F}_{int,G}^{e}}{\partial \overline{\overline{\mathbf{d}}}_e}(t) = \int_{\Omega_e} \overline{\mathbf{G}}_v^T(\mathbf{x})\frac{\partial \mathbf{F}}{\partial \tilde{\boldsymbol{\varepsilon}}}(\mathbf{x},t)\overline{\mathbf{G}}_r(\mathbf{x})d\Omega_e + \frac{\partial \mathbf{t}}{\partial \overline{\overline{\mathbf{d}}}_e}(t)l_{\Gamma_d} \tag{80}$$

with $\mathbf{t}$ the cohesion forces defined as:

$$\mathbf{t}(t) = \mathbf{F}(\mathbf{x}_d,t) = \mathbf{F}(\mathbf{x},t)|_{\Gamma_d} \quad \text{and} \quad \begin{bmatrix}\mathbf{t}_u(t)\\ \mathbf{t}_\theta(t)\end{bmatrix} = \begin{bmatrix}\mathbf{N}(\mathbf{x}_d,t)\\ \mathbf{M}(\mathbf{x}_d,t)\end{bmatrix} \tag{81}$$

Therefore, we have:

$$\frac{\partial \mathbf{t}}{\partial \overline{\overline{\mathbf{d}}}_e}(t) = \begin{bmatrix}\frac{\partial \mathbf{t}_u}{\partial \overline{\overline{\mathbf{U}}}}(t) & \frac{\partial \mathbf{t}_u}{\partial \overline{\overline{\boldsymbol{\Theta}}}}(t)\\ \frac{\partial \mathbf{t}_\theta}{\partial \overline{\overline{\mathbf{U}}}_e}(t) & \frac{\partial \mathbf{t}_\theta}{\partial \overline{\overline{\boldsymbol{\Theta}}}_e}(t)\end{bmatrix} = \begin{bmatrix}\frac{\partial \mathbf{t}_u}{\partial \overline{\overline{\mathbf{U}}}_e}(t) & 0\\ 0 & \frac{\partial \mathbf{t}_\theta}{\partial \overline{\overline{\boldsymbol{\Theta}}}_e}(t)\end{bmatrix} \tag{82}$$

The cohesive models governing the membrane and bending behaviors at the discontinuity line Γ_d are assumed to be uncoupled. Coupling is possible if a staggered static condensation strategy is used [25]. The assembly of the local equations (79) and (80) over all elements gives:

$$\mathop{\mathrm{A}}_{e=1}^{n}\begin{bmatrix}\mathbf{K}_{GB} & \mathbf{K}_{GG}\end{bmatrix}_{t+1}^{(k)}\begin{bmatrix}\Delta\mathbf{d}_e^{(k)}\\ \Delta\overline{\overline{\mathbf{d}}}_e^{(l+1)}\end{bmatrix}_{t+1} = -\mathbf{F}_{int,G}{}_{t+1}^{e,(l)} \tag{83}$$

Combining equations (76) and (83) results in:

$$\mathop{\mathrm{A}}_{e=1}^{n}\begin{bmatrix}\mathbf{K}_{BB} & \mathbf{K}_{BG}\\ \mathbf{K}_{GB} & \mathbf{K}_{GG}\end{bmatrix}_{t+1}^{(l)}\begin{bmatrix}\Delta\mathbf{d}_e\\ \Delta\overline{\overline{\mathbf{d}}}_e\end{bmatrix}_{t+1}^{(k+1)} = \begin{bmatrix}-(\mathbf{F}_{int,B}^{e} - \mathbf{F}_{ext}^{e})\\ -\mathbf{F}_{int,G}^{e}\end{bmatrix}_{t+1}^{(k)} \tag{84}$$

The resulting system (84) can be solved by performing static condensation at the finite element level. This technique allows to solve the enhancement variables at the local level [26]. Once the equilibrium at the discontinuity line is reached, the value of $\mathbf{F}_{int,G}^{e}|_{t+1}$ is canceled. Hence:

$$\mathop{\mathrm{A}}_{e=1}^{n}\begin{bmatrix}\mathbf{K}_{BB} & \mathbf{K}_{BG}\\ \mathbf{K}_{GB} & \mathbf{K}_{GG}\end{bmatrix}_{t+1}^{(l)}\begin{bmatrix}\Delta\mathbf{d}_e\\ \Delta\overline{\overline{\mathbf{d}}}_e\end{bmatrix}_{t+1}^{(k+1)} = \begin{bmatrix}-(\mathbf{F}_{int,B}^{e} - \mathbf{F}_{ext}^{e})\\ \mathbf{0}\end{bmatrix}_{t+1}^{(k)} \tag{85}$$

The second equation of this system gives:

$$\left[\mathbf{K}_{GB}|^{(l)}\,\Delta\mathbf{d}_e + \mathbf{K}_{GG}|^{(l)}\Delta\overline{\overline{\mathbf{d}}}_e\right]_{t+1}^{(k+1)} = 0$$

thus:

$$\Delta\overline{\overline{\mathbf{d}}}_e|_{t+1}^{(k+1)} = -\mathbf{K}_{GG}^{-1}|^{(l)}\,\mathbf{K}_{GB}|^{(l)}\,\Delta\mathbf{d}_e|_{t+1}^{(k+1)} \tag{86}$$

The expression of $\Delta\overline{\overline{\mathbf{d}}}_e|_{t+1}^{(k+1)}$ is introduced into the first equation of the system (85) to give:

$$\begin{aligned}&\mathbf{K}_{BB}|^{(l)}\ \Delta\ \mathbf{d}_e|_{t+1}^{(k+1)}+\mathbf{K}_{BG}|^{(l)}(-\mathbf{K}_{GG}^{-1}|^{(l)}\ \ \mathbf{K}_{GB}|^{(l)}\ \Delta\mathbf{d}_e)|_{t+1}^{(k+1)}\\&=-(\mathbf{F}_{int,B}^{e}-\mathbf{F}_{ext}^{e})|_{t+1}^{(k+1)}\end{aligned}\tag{87}$$

And then:

$$\begin{aligned}&\underbrace{\left(\mathbf{K}_{BB}|^{(l)}-\mathbf{K}_{BG}|^{(l)}\ \mathbf{K}_{GG}^{-1}|^{(l)}\ \mathbf{K}_{GB}|^{(l)}\right)}_{\mathbf{K}_{cond}^{e}|^{(l)}}\Delta\mathbf{d}_e|_{t+1}\\&=-\left(\mathbf{F}_{int,B}^{e}-\mathbf{F}_{ext}^{e}\right)|_{t+1}^{(k+1)}\end{aligned}\tag{88}$$

with $\mathbf{K}_{cond}^{e}$ the condensed stiffness matrix. The main advantage of the static condensation method is that the total number of degrees of freedom at the structure level remains unchanged. This matrix can be updated during iterations with the evolution of the material state. This reduces the number of iterations and then shortens the computation time; however, it can sometimes lead to snap-back numerical instabilities. In this case, it is necessary to refer to advanced displacement/load control techniques such as the arc length method [27].

4.2. Geometrical transformation

It is necessary to distinguish three systems of axes, see Fig.5. The first one is the global system of axes. It is also known as the physical one. The second one is a local system of axes which is defined at the element level whose origin is represented by the first node belonging to the element according to the connectivity table. The third system of axis is local and is defined at the discontinuity line level which has the advantage of managing the local equilibrium of the element in a scalar way and particularly to check the discontinuity activation. Therefore, it is necessary to pay attention to perform transformations between the different systems during the computation in a proper way. Furthermore, an additional transformation into the reference finite element is necessary during numerical integration step using, for instance, the Gauss method. Details about these geometrical transformations can be found in [28].

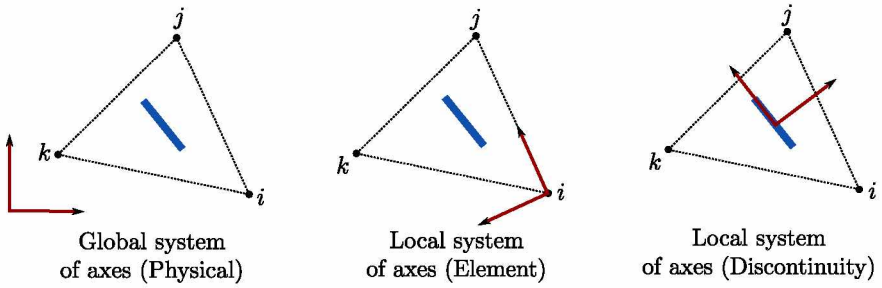

Figure 5: The different system of axes.

5. Numerical applications

5.1. Description of the numerical setting

In order to study the membrane and bending discontinuity independently and to prove the relevancy of the proposed modeling strategy, a square-shaped plate with a size of 1×1 m^2 is considered, as shown in Fig.6. The thickness of the plate is assumed to be constant and equal to 1 m. The structure is discretized into two triangular elements of T3γ type. Nodes P2 and P3 are fixed. Nodes P3 and P4 are free to move. For the membrane component, the constitutive model used is non-symmetrical: elastic-cohesive in tension and linear elastic in compression. However, for the bending component, the constitutive model is symmetrical elastic-cohesive. The material parameters are summarized in table (1).

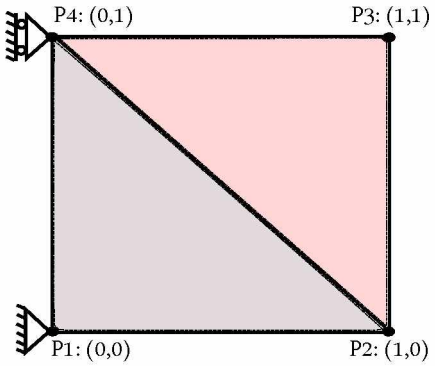

Figure 6: Geometry and mesh size of the plate.

Young's modulus	Poisson's ratio	Fracture surface energy	Threshold limit
E	ν	G_m & G_f	N_u
3×10^{10}	0.2	10^3 & 5×10^3	2.8×10^6
Pa	-	$\mathrm{N.m^{-2}}$	$\mathrm{N.m^{-1}}$

Table 1: Material parameters.

5.2. Elementary tests

5.2.1. Pure membrane behavior under cyclic loading

The first test aims to study of the plate under pure tension. It consists in imposing an axial displacement U_x on the nodes P2 and P3. Time evolution of the loading is given in Fig.7. The global response of the plate is shown in Fig.8. It shows the cyclic behavior of

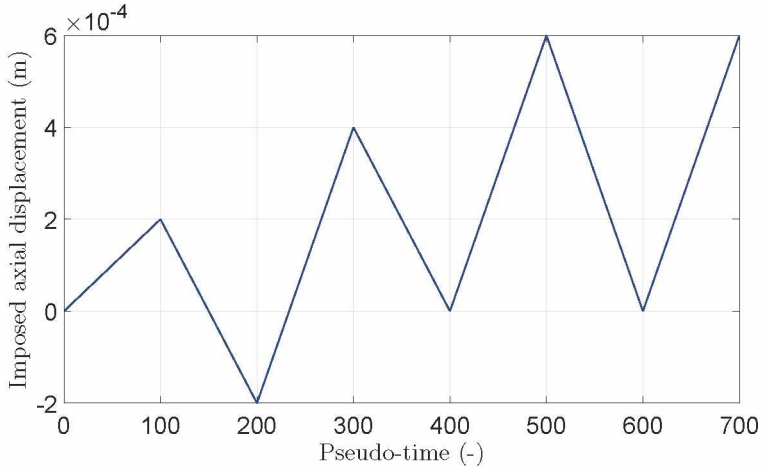

Figure 7: The time evolution of the loading.

the membrane component. The discontinuity opens and closes during each cycle. As expected, in compression, the behavior is linear elastic. This validates the proper implementation of the enhanced plate model for the membrane component. The crack discontinuity vs. traction vector evolution related to the membrane part is shown in Fig.9. The exponential shape of the curve is consistent with the traction-separation law used.

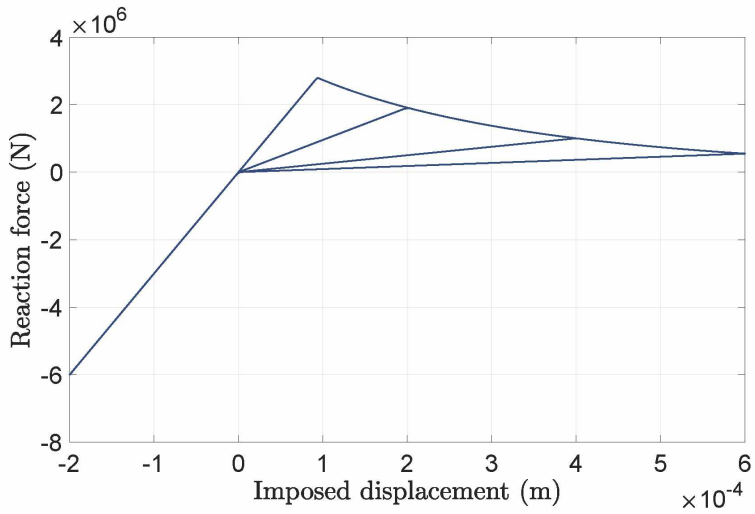

Figure 8: Global response: reaction force vs. imposed displacement.

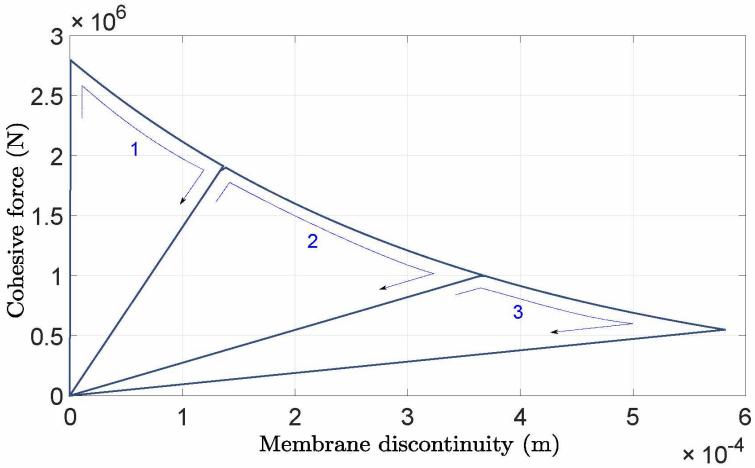

Figure 9: Cohesive response: cohesive force vs. discontinuity. The arrows in the figure (in blue) with the associated numbers allow to clarify the loading path.

An element fails when a discontinuity is opened inside it and its maximum value is reached, so that the force is no longer transferred between the lips. This state is known as fully softened discontinuity. Fig.10 qualitatively illustrates the evolution of the plate state: before discontinuities activation, after their activation and at element failure.

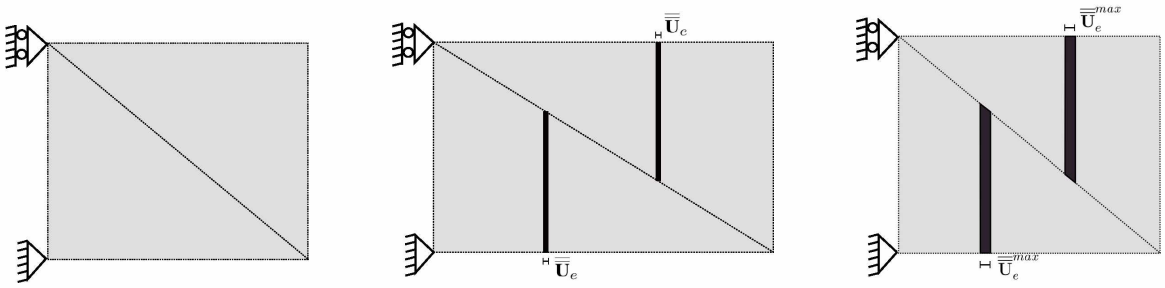

(a) Representation of the structure before the activation of the discontinuities.

(b) Representation of the structure after the activation of the discontinuities.

(c) Representation of the structure at the fully softened discontinuities.

Figure 10: Evolution of the state of the elements.

5.2.2. Pure bending behavior under cyclic loading

The second test consists in imposing a pure rotation. The same numerical setting as the one previously presented is considered. A rotation is imposed at the degrees of freedom Θ_y at nodes P2 and P3 according to Fig.11. It is necessary to pay attention to the fact that the rotation Θ_y influences the curvature κ_x and therefore the moment M_x. A similar effect is observed for Θ_x and M_y. The global

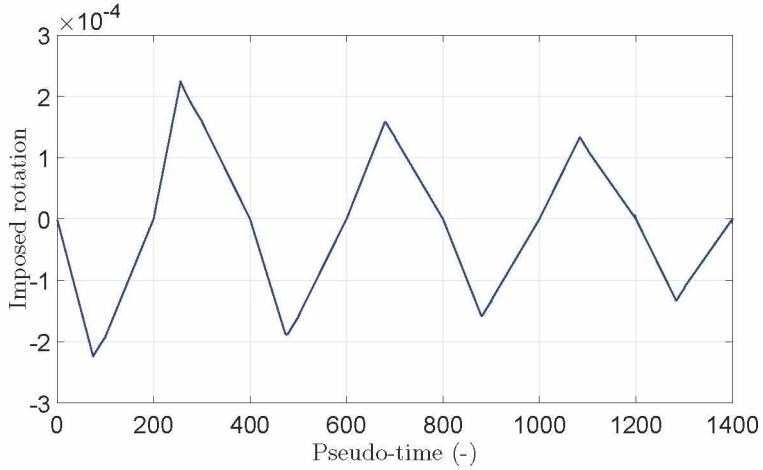

Figure 11: Time evolution of the loading.

response of the plate in pure bending is illustrated in figure (12). The crack opening vs. the traction vector evolution is shown in Fig.13.

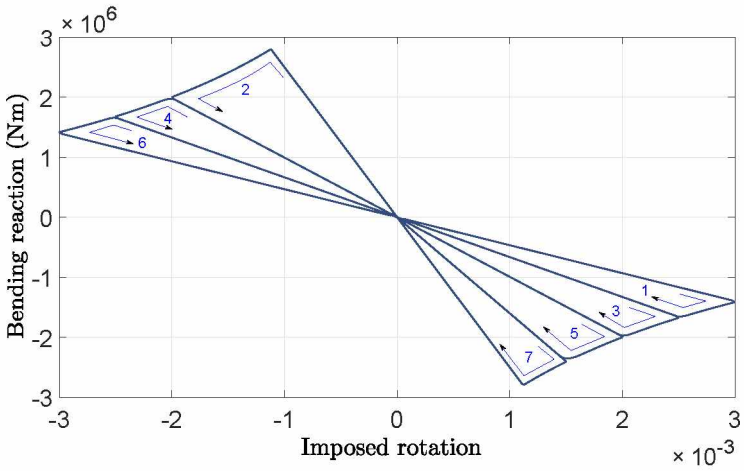

Figure 12: Global response: bending force vs. imposed rotation. The arrows in the figure (in blue) with the associated numbers allow to clarify the loading path.

This result validates the cohesive damage model that is used.

5.2.3. Simultaneous activation of both discontinuities

In order to study how the proposed model works when two discontinuities are simultaneously activated, we consider the square plate of the previous example and we apply parallel loading, as shown in Fig.14. On one hand, an axial displacement is applied up to a maximum value (5×10^{-4} m) and then is kept constant. Simultaneously, a rotation is cyclically imposed between two opposite values ($\pm 5 \times 10^{-3}$). Both loads are applied at P2 and P3 nodes. The results obtained are illustrated in Fig.15. They show that the plate model can develop two discontinuities simultaneously without any numerical instabilities. Fig.15a shows the overall response of the membrane component and Fig.15b shows the overall behavior of the bending components.

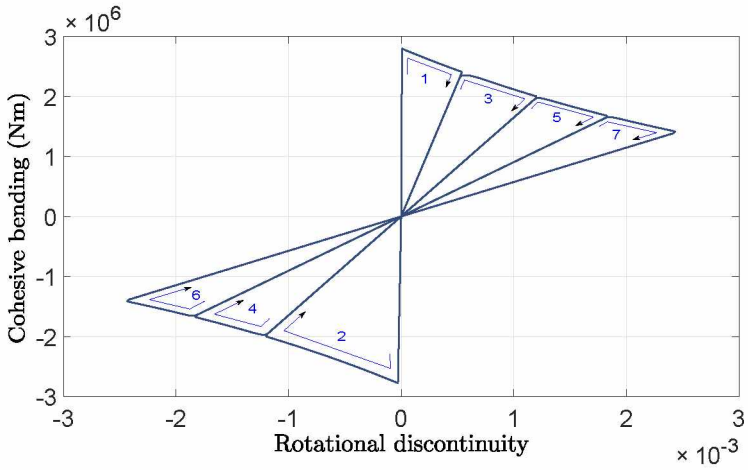

Figure 13: Cohesive response: cohesive bending vs. rotation discontinuity. The arrows in the figure (in blue) with the associated numbers allow to clarify the loading path.

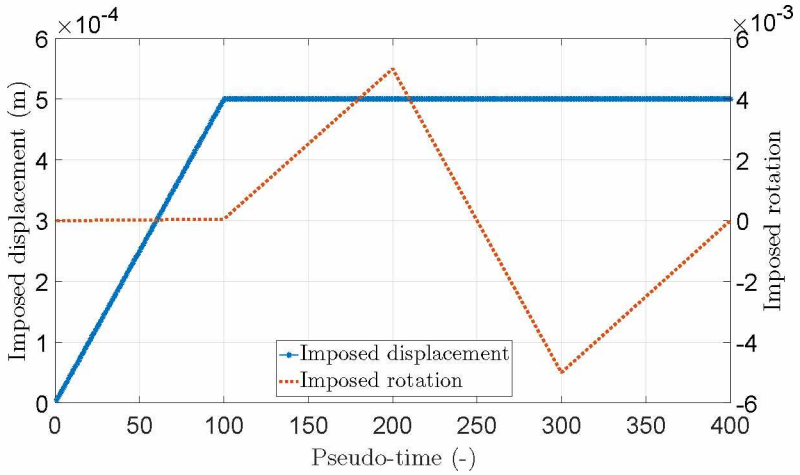

Figure 14: Time evolution of the loading history.

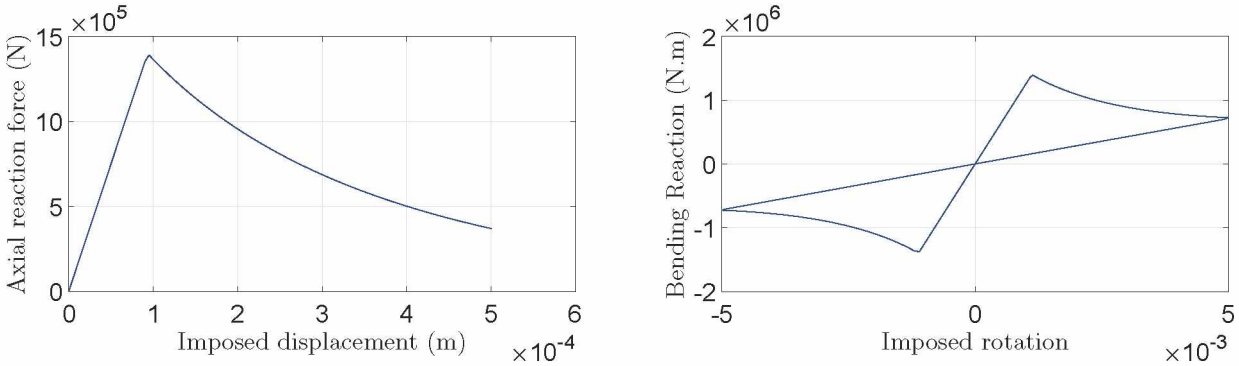

(a) Membrane response

(b) bending response

Figure 15: Global responses.

5.3. Mesh sensitivity study

A mesh sensitivity study has been performed and the results are shown in this section. A localization band of width L is defined in the middle of the plate represented by the light blue area in Fig.16. The localization band refers to the position where discontinuities are activated. Outside of this zone, the material behavior remains linear elastic. Regarding the boundary conditions, the vertical side joining

the nodes P1 and P4 of the plate is embedded and the loads are applied on the vertical side joining the nodes P2 and P3 at the right boundary of the plate. Two simulation groups are carried out. The first group consists in imposing an axial displacement according to U_x

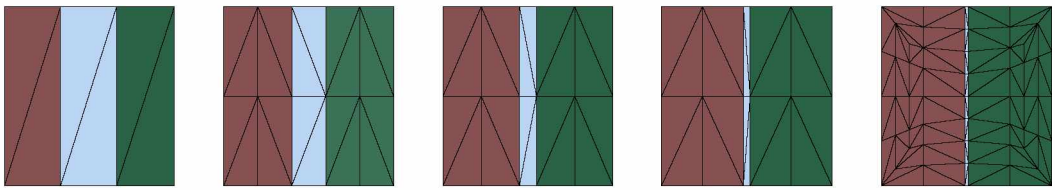

(a) L=0.33; n_e=6 (b) L=0.20; n_e=20 (c) L=0.10; n_e=20 (d) L=0.04; n_e=20 (e) L=0.02; n_e=112

Figure 16: The different mesh sizes where n_e is the number of elements.

in order to study the membrane response with respect to mesh size. The second group consists in imposing a rotation according to Θ_y in order to study the bending response as a function of the mesh size. The results from the two simulation groups are shown in figure (17). These results show that the proposed model is free of mesh-dependency effects. It can be noticed this result was expected due to the fact that the E-FEM is used.

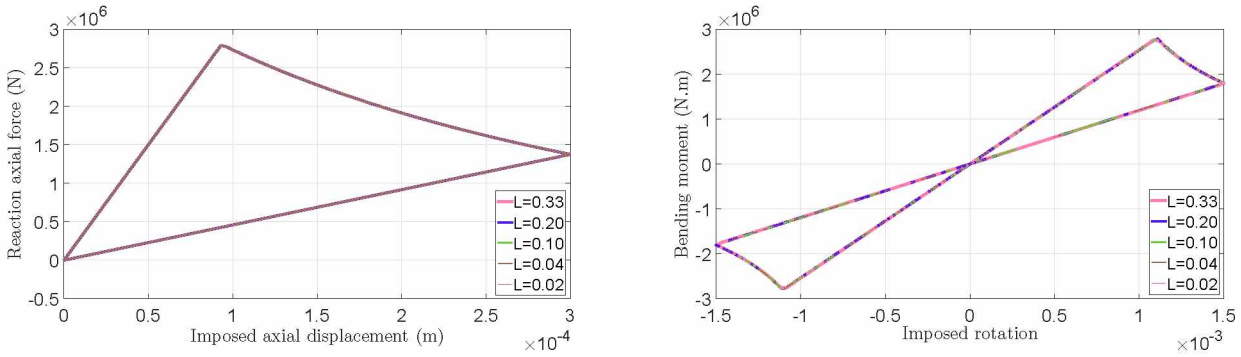

(a) Pure membrane responses. (b) Pure bending responses.

Figure 17: Global responses according to mesh size.

5.4. Willam's Test

The Willam's test [29] refers to a numerical test that aims to study the numerical robustness of the local integration scheme and to investigate the model's ability to describe induced anisotropy. In [30], the test was used to describe and compare the rotating and fixed crack models. Also, in [31] an analysis of different constitutive models is performed in order to assess their performances to deal with mixed mode cracking. The test is now widely used to check that no numerical instabilities are encountered in case of a complex 3D damage models of concrete [32].

In this work, the realization of the Willam's test is inspired from the work of [33] and is performed for both the membrane and bending components.

As shown in Fig.18, the test is divided into two stages: In the first stage, a uniaxial load strain is applied in the x-direction accompagnied by lateral Poisson contraction in the y-direction such that the strain increments Δe_x, Δe_y and Δe_{xy} evolve respectively according to the portions 1, $-\nu$, 0. When the material reaches the tension threshold, which in this case represents the maximum stress value, the discontinuity is activated. Then, in the second stage, a shear loading strain is applied such that the strain increments Δe_x, Δe_y and Δe_{xy} henceforth evolve respectively according to the proportions 1, 1.5, 1, while the out-of-plane degrees of freedom remain unchanged. The material parameters are the same as those of the first numerical tests, as shown in table (1).

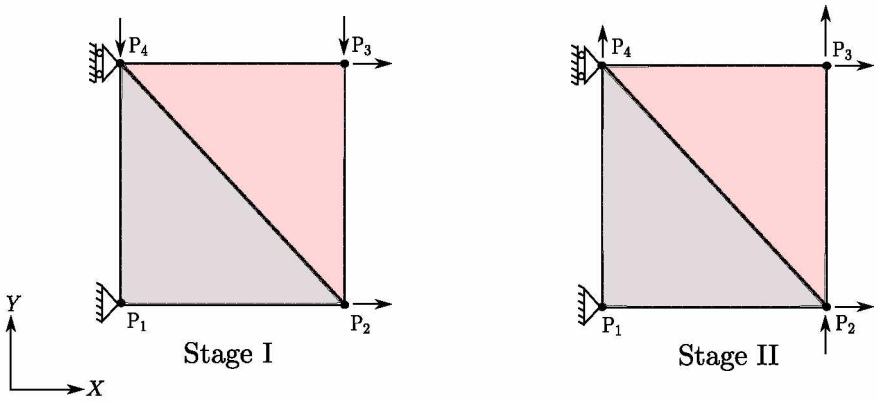

Figure 18: Willam's test configuration.

5.4.1. Membrane behavior

The test was first performed for the membrane behavior. The evolution of the three strain components is illustrated in Fig.19 to ensure that the proportions are respected. Then, the evolution of the three stress components (N_x, N_y and N_{xy}) associated with the three

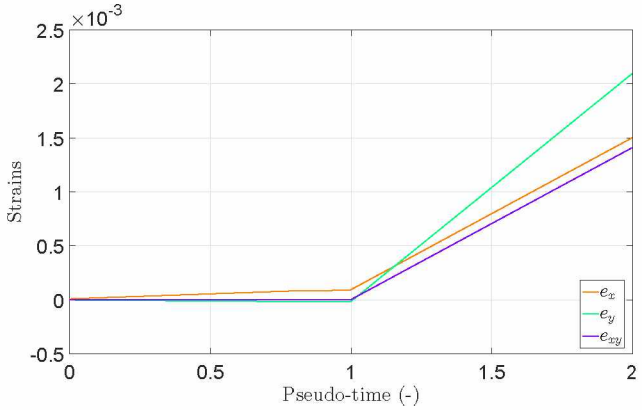

Figure 19: Time evolution of the strain components e_x, e_y and e_{xy}.

membrane strains (e_x, e_y and e_{xy}) are shown in Fig.20 as a function of the axial strain (e_x). Once the peak level is reached, the shear response begins while continuing to apply the loading.

The results shown in Fig.20 show that the Willam test is successful. The stress N_y is linear as shown in Fig.20; this is due to the fact that the model does not take into account multi-cracking [33]. In this instance, the normal to the discontinuity line is assumed to be fixed for once oriented along the x-axis. In addition, regarding the linearity obtained for the N_{xy} component in Fig.20, this is due to the fact that there is no sliding between the crack surfaces. Accordingly, even if there is no softening in the behaviors of N_y and N_{xy}, numerical robustness is still demonstrated since continuity in the stress-strain relationship as well as softening are well preserved. These effects can be achieved by implementing a more complex cohesive law [21]; however, this is not the primary focus of our work, which is to provide a digital framework.

A final outcome lies in the rotations of the principal axes of stresses and strains with respect to the physical system of axis and is shown in Fig.21. We note that the angles of rotation of the systems of principal axes are not the same for stresses and strains. This means that anisotropy is induced since the constitutive models used are initially isotropic and, in this case, the angles are supposed to be the same. Therefore, one can conclude that the apparent anisotropy is induced by the development of discontinuity within the element. The anisotropy rate can be quantified by the ratio between the two asymptotic values of the angle and is equal to $\frac{75-50}{75} \times 100 = 33\%$. If we compare this value to what [33] has obtained, i.e. 46%, we notice a difference due to the fact that the initial model used in [33] is

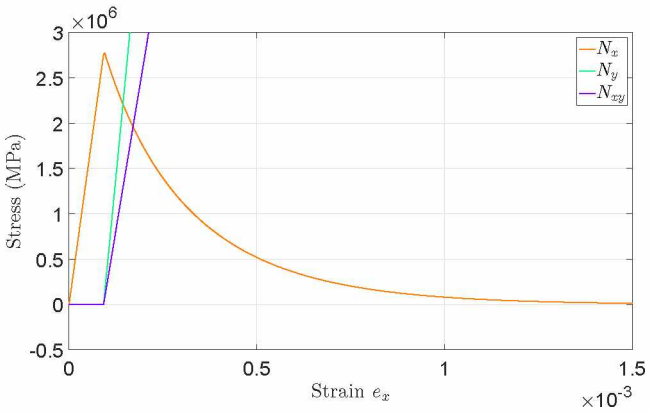

Figure 20: Stresses evolution with respect to strain e_x.

intrinsically anisotropic. This explains why anisotropy is more significant in their case.

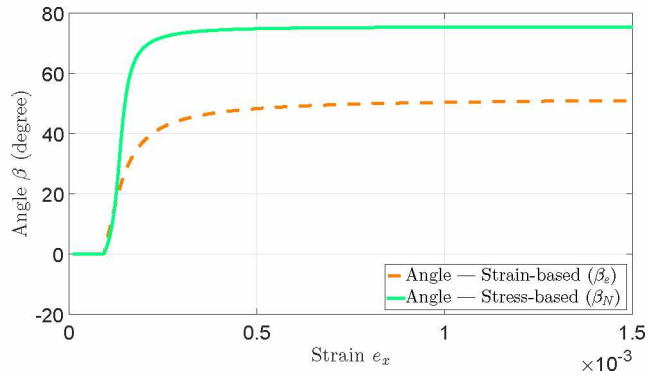

Figure 21: Evolution of the angle of principal stress and strain direction with respect to strain e_x.

5.4.2. Bending behavior

Another novelty characterizing the results shown in this work is the execution of the Willam's test on the plate bending behavior. Thus, instead of applying a load in the membrane part, a load affecting the bending part is applied. The loading protocol has been kept unchanged with respect to the case of the membrane part, see Fig.22. The same analysis as the one performed in the previous application

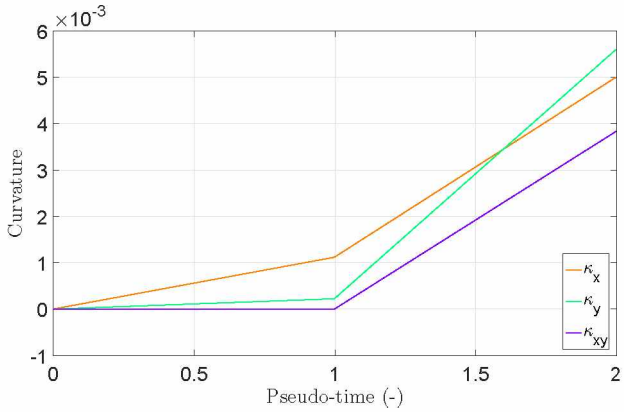

Figure 22: Curvature components evolution with respect to pseudo-time.

has been made. The shear response starts as soon as the bending moment limit value is reached and the rotation discontinuity is activated. It is obvious in Fig.23 that the relationship between the bending moment M_x and the bending curvature κ_x remains continuous with a

proper softening phase. On the other hand, the bending moment M_y evolves in a linear elastic way since multi-cracking is not taken into account. In addiction, the M_{xy} increases elastically because the sliding at the discontinuity level is neglected. Finally, the evolution of

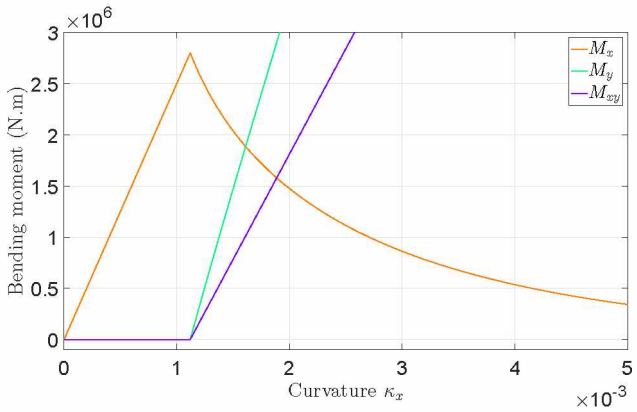

Figure 23: Bending stresses evolution with respect to curvature κ_x.

the angles of the principal axes for bending moments and curvatures is illustrated in Fig.24. This figure shows that the discontinuity of rotation induces an anisotropy. This result shows that anisotropy is also developing in the bending part.

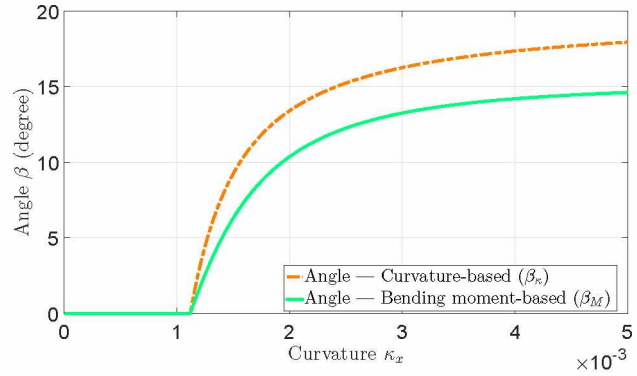

Figure 24: Evolution of the angle of principal bending stress and curvature direction with respect to curvature κ_x.

5.5. Discussion: model limitations and perspectives

The main objective of the paper is to present in a clear, didactic and self-supporting way the theoretical framework of a new thick plate model allowing to have two discontinuities of membrane and flexion. The previous elementary test cases were presented to verify the concept of the model and to show how the model works on elementary cases.

After verifying the functionality of the model, it is necessary to validate the model against reference results: analytical or experimental results. However, the model requires additional development in order to ensure the C^0 continuity of the crack path through adjacent finite elements. A reflection in that direction still has to be carried out. More precisely, the tracking strategy to be adopted in order to ensure a continuation of the crack's propagation within the elements has to be defined and reveisited with respect to existing ones. In fact, crack path strategies are still under discussion within the framework of the Embedded Finite Element Method. To overcome this issue, the embedded finite element method can be combined with tracking algorithms to provide a propagation path continuity that allows to raise the loss of objectivity that may occur during simulations. Local or global tracking algorithms can be found in literature [34]. What differs mainly between the two methods is the way in which the direction of the discontinuity propagation is determined. Local approaches allow the reproduction of continuous crack paths by analyzing information from adjacent elements. However, using them in the case of

multiple crack problems can be difficult and this strategy may lose a high portion of its robustness. In order to overcome the limitations of local strategies, global approaches have been developed to be able to model the multi-crack problem robustly [35].

Several developments have been performed to study the crack path continuity within the framework of conventional finite element models whose discontinuity is introduced into the displacement field. However, for rotational discontinuities, this has never been studied to the best of the authors' knowledge. In addition, since the proposed enhanced model allows the development of two membrane and rotation discontinuities, the choice of tracking strategy is more challenging and needs to be studied separately in order to determine which approach is the most appropriate. This step is necessary to be able to perform large-scale and self-supporting simulations in which crack propagation will occur. After that, more complex cases will be needed to assess the model's ability to reproduce experimental reference results that are representative of real engineering structures. Indeed, this is one of our objectives for futher works.

6. Conclusions

In this paper, a theoretical formulation of a *Mindlin-Reissner* plate with enhanced kinematics is presented. The main purpose of the enhancement is to take into account the behavior of a structure up to failure by correctly describing the strain localization that accompanies the softening phase. The membrane displacement and rotation fields are enhanced with two discontinuities. The discontinuities are incorporated into the element by means of the *Embedded Finite Element Method*. The compatibility and equilibrium operators associated with the two discontinuities are determined. The enhanced kinematic of the model allows to always detect a quantity of dissipated energy unlike the classical continuous model (stress vs. strain) with a softening phase. As a result, the model is low mesh-dependent. The linearization of the equilibrium equations, the computational procedure are addressed. Several case studies are presented to demonstrate the relevancy of the element and its ability to reproduce the behavior until failure independently of the mesh size. The Willam's test is also performed to verify the robustness of the integration path and quantify the anisotropy rate related to the formulation. In summary, three main novelties characterize the work carried out in the context of this paper. First, the proposed Mindlin-Reissner plate element is based on a simplified kinematic assumption that reduces the number of degrees of freedom compared to three-dimensional approaches. In addition, it consists of a three-node linear triangular element that is adjusted to overcome the shear locking and therefore requires a single integration point in the calculation. The motivation behind this choice is to provide engineers with a fast and efficient modeling tool. Second, a double discontinuity (membrane, bending) is introduced and allows the introduction of two distinct or coupled generalized cohesive laws (membrane, bending). The Authors have planned to study this point in a future work. Third, the model allows for good control of unilateral conditions; indeed, it is able to recover the material's stiffness in compression previously damaged in tension. On the other hand, in order to reproduce the shear failure, it is necessary to enhance the transverse displacement field with a supplementary discontinuity variable. This issue is significant and could be addressed in future works. Finally, a very important challenge is the extension of this work to the context of multilayerd plates. This allows working with material constitutive models instead of dealing with generalized models. The plate can then be made of various materials and each material can be modelled by a specific constitutive model. This allows the evolution of damage at the cross-section level to be closely tracked.

Acknowledgements

The authors would like to thank the ILISBAR project (Identification du comportement ds Liaisons d'une Structure BA dans le cas d'un Renforcement parasismique), funded by the French National Agency of Research under Grant ANR-16-CE22-0002.

References

[1] D. R. J. Owen, E. Hinton, Finite elements plasticity: Theory and Practice, Pineridge Press Limited, 1980.

[2] S. Liu, T. Yu, L. Van Lich, S. Yin, T. Q. Bui, Size effect on cracked functional composite micro-plates by an xiga-based effective approach, Meccanica 53 (10) (2018) 2637–2658.

[3] A. Giampieri, U. Perego, An interface finite element for the simulation of localized membrane-bending deformation in shells, Computer Methods in Applied Mechanics and Engineering 200 (29-32) (2011) 2378–2396. doi:10.1016/j.cma.2011.04.009.

[4] J. Dolbow, N. Moës, T. Belytschko, Modeling fracture in Mindlin–Reissner plates with the extended finite element method, International journal of solids and structures 37 (48-50) (2000) 7161–7183.

[5] J. Lasry, J. Pommier, Y. Renard, M. Salaün, extended finite element methods for thin cracked plates with kirchhoff–love theory, International Journal for Numerical Methods in Engineering 84 (9) (2010) 1115–1138.

[6] E. N. Dvorkin, a. M. Cuitiño, G. Gioia, Finite elements with displacement interpolated embedded localization lines insensitive to mesh size and distortions, International Journal For Numerical Methods In Engineering 30 (September 1989) (1990) 541–564. doi:10.1002/nme.1620300311.

[7] T. Belytschko, J. Fish, Embedded hinge lines for plate elements, Computer Methods in Applied Mechanics and Engineering 76 (1) (1989) 67–86. doi:10.1016/0045-7825(89)90141-2.

[8] F. Armero, D. Ehrlich, Finite element methods for the multi-scale modeling of softening hinge lines in plates at failure, Computer Methods in Applied Mechanics and Engineering 195 (13-16) (2006) 1283–1324.

[9] F. Armero, Strong discontinuities in antiplane/torsional problems of computational failure mechanics, International journal of fracture 178 (1-2) (2012) 3–32.

[10] B. Richard, G. Rastiello, C. Giry, F. Riccardi, R. Paredes, E. Zafati, S. Kakarla, C. Lejouad, Castlab: an object-oriented finite element toolbox within the matlab environment for educational and research purposes in computational solid mechanics, Advances in Engineering Software 128 (2019) 136–151.

[11] F. Armero, K. Garikipati, An analysis of strong discontinuities in multiplicative finite strain plasticity and their relation with the numerical simulation of strain localization in solids, International Journal of Solids and Structures 33 (20-22) (1996) 2863–2885.

[12] O. Zienkiewicz, R. Taylor, J. Too, Reduced integration technique in general analysis of plates and shells, International Journal for Numerical Methods in Engineering 3 (2) (1971) 275–290.

[13] T. J. R. Hughes, R. L. Taylor, W. Kanoknukulchais, A simple and efficient finite element for plate bending, International Journal for Numerical Methods in Engineering 11 (May 1976) (1977) 1529–1543. doi:10.1002/nme.1620111005.

[14] C. Lovadina, Analysis of a mixed finite element method for the reissner-mindlin plate problems, Computer Methods in Applied Mechanics and Engineering 163 (1-4) (1998) 71–85.

[15] T. J. Hughes, T. Tezduyar, Finite elements based upon mindlin plate theory with particular reference to the four-node bilinear isoparametric element, Journal of applied mechanics 48 (3) (1981) 587–596.

[16] A. Ibrahimbegović, F. Frey, Finite element analysis of linear and non-linear planar deformations of elastic initially curved beams, International Journal for Numerical Methods in Engineering 36 (19) (1993) 3239–3258. doi:10.1002/nme.1620361903.

[17] J. Mosler, G. Meschke, 3D modelling of strong discontinuities in elastoplastic solids: Fixed and rotating localization formulations, International Journal for Numerical Methods in Engineering 57 (11) (2003) 1553–1576. doi:10.1002/nme.731.

[18] B. Richard, E. Kishta, C. Giry, F. Ragueneau, Strong discontinuity analysis of a class of anisotropic continuum damage constitutive models Part I: Theoretical considerations, Mechanics Research Communications 86 (2017) 32–36. doi:10.1016/j.mechrescom.2016.09.010.

[19] I. Bitar, P. Kotronis, N. Benkemoun, S. Grange, A generalized Timoshenko beam with embedded rotation discontinuity, Finite Elements in Analysis and Design 150 (2018) 34–50. doi:10.1016/j.finel.2018.07.002.

[20] G. Rastiello, F. Riccardi, B. Richard, Discontinuity-scale path-following methods for the embedded discontinuity finite element modeling of failure in solids, Computer Methods in Applied Mechanics and Engineering 349 (2019) 431–457. doi:10.1016/j.cma.2019.02.030.

[21] J. Alfaiate, G. Wells, L. Sluys, On the use of embedded discontinuity elements with crack path continuity for mode-i and mixed-mode fracture, Engineering fracture mechanics 69 (6) (2002) 661–686.

[22] I. Bitar, N. Benkemoun, P. Kotronis, S. Grange, A multifiber Timoshenko beam with embedded discontinuities, Engineering Fracture Mechanics 214 (2019) 339–364.

[23] C. Linder, F. Armero, Finite elements with embedded strong discontinuities for the modeling of failure in solids, International Journal for Numerical Methods in Engineering 72 (12) (2007) 1391–1433.

[24] R. L. Taylor, J. C. Simo, O. C. Zienkiewicz, a. C. H. Chan, The patch testa condition for assessing FEM convergence, International Journal for Numerical Methods in Engineering 22 (1) (1986) 39–62. doi:10.1002/nme.1620220105.

[25] J. Simo, F. Armero, R. Taylor, Improved versions of assumed enhanced strain tri-linear elements for 3d finite deformation problems, Computer methods in applied mechanics and engineering 110 (3-4) (1993) 359–386.

[26] E. L. Wilson, The static condensation algorithm, International Journal for Numerical Methods in Engineering 8 (1) (1974) 198–203. doi:10.1002/nme.1620080115.
URL http://doi.wiley.com/10.1002/nme.1620080115

[27] H.-B. Hellweg, M. Crisfield, A new arc-length method for handling sharp snap-backs, Computers & Structures 66 (5) (1998) 704–709.

[28] S. Potapov, Éléments de plaque : Modélisation Q4GG, Documentation code Aster R3.07.09.

[29] K. Willam, E. Pramono, S. Sture, Fundamental issues of smeared crack models, in: Fracture of concrete and rock, Springer, 1989, pp. 142–157.

[30] P. Feenstra, R. de Borst, J. G. Rots, A comparison of different crack models applied to plain and reinforced concrete, Fracture Processes in Concrete, Rock and Ceramics.

[31] P. Pivonka, J. Ožbolt, R. Lackner, H. A. Mang, Comparative studies of 3D-constitutive models for concrete: Application to mixed-mode fracture, International Journal for Numerical Methods in Engineering 60 (2) (2004) 549–570. doi:10.1002/nme.975.

[32] M. Chambart, R. Desmorat, F. Gatuingt, Intrinsic dissipation of a modular anisotropic damage model: application to concrete under impact, Engineering Fracture Mechanics 127 (2014) 161–180.

[33] E. Kishta, B. Richard, C. Giry, F. Ragueneau, Strong discontinuity analysis of a class of anisotropic continuum damage constitutive models–part ii: Concrete material application, Mechanics Research Communications 86 (2017) 27–31.

[34] J. Oliver, A. Huespe, E. Samaniego, E. Chaves, On strategies for tracking strong discontinuities in computational failure mechanics, in: Fifth World Congress on Computational Mechanics, 2002, pp. 7–12.

[35] F. Riccardi, E. Kishta, B. Richard, A step-by-step global crack-tracking approach in e-fem simulations of quasi-brittle materials, Engineering Fracture Mechanics 170 (2017) 44–58.

AppendixA. Generalized behaviour of the plate

In order to obtain a generalized form of the plate behavior, the generalized force equations (10) are developed according to the material behavior law (15). For membrane forces **N**, we have:

$$\mathbf{N} = \int_{\frac{-h}{2}}^{\frac{h}{2}} \boldsymbol{\mathcal{S}}_p dz = \mathbf{H}_m \mathbf{e} + \mathbf{H}_{mf} \boldsymbol{\kappa} \tag{A.1}$$

with:

$$\mathbf{H}_m = \int_{\frac{-h}{2}}^{\frac{h}{2}} \mathbf{H} dz \quad \text{and} \quad \mathbf{H}_{mf} = \int_{\frac{-h}{2}}^{\frac{h}{2}} z\mathbf{H} dz \tag{A.2}$$

$\mathbf{H}_{mf}$ takes a zero value in case of a symmetrical section whose axis is taken at the level of the midplane. In the same way, we proceed for the bending components:

$$\mathbf{M} = \int_{\frac{-h}{2}}^{\frac{h}{2}} z\boldsymbol{\mathcal{S}}_p dz = \mathbf{H}_{mf} \mathbf{e} + \mathbf{H}_f \boldsymbol{\kappa} \tag{A.3}$$

with:

$$\mathbf{H}_f = \int_{\frac{-h}{2}}^{\frac{h}{2}} z^2 \mathbf{H} dz \tag{A.4}$$

Finally, the same step is done for the shear component such as:

$$\mathbf{T} = \int_{\frac{-h}{2}}^{\frac{h}{2}} \boldsymbol{\mathcal{S}}_z dz = \mathbf{H}_{ct} \boldsymbol{\gamma} \tag{A.5}$$

with:

$$\mathbf{H}_{ct} = \int_{\frac{-h}{2}}^{\frac{h}{2}} \mathbf{H}_{\boldsymbol{\gamma}} dz \tag{A.6}$$